Noise radiation of a low Reynolds number propeller at an angle of attack.

An experimental and analytical study.

D.W. van Hoogstraten

MSc thesis report

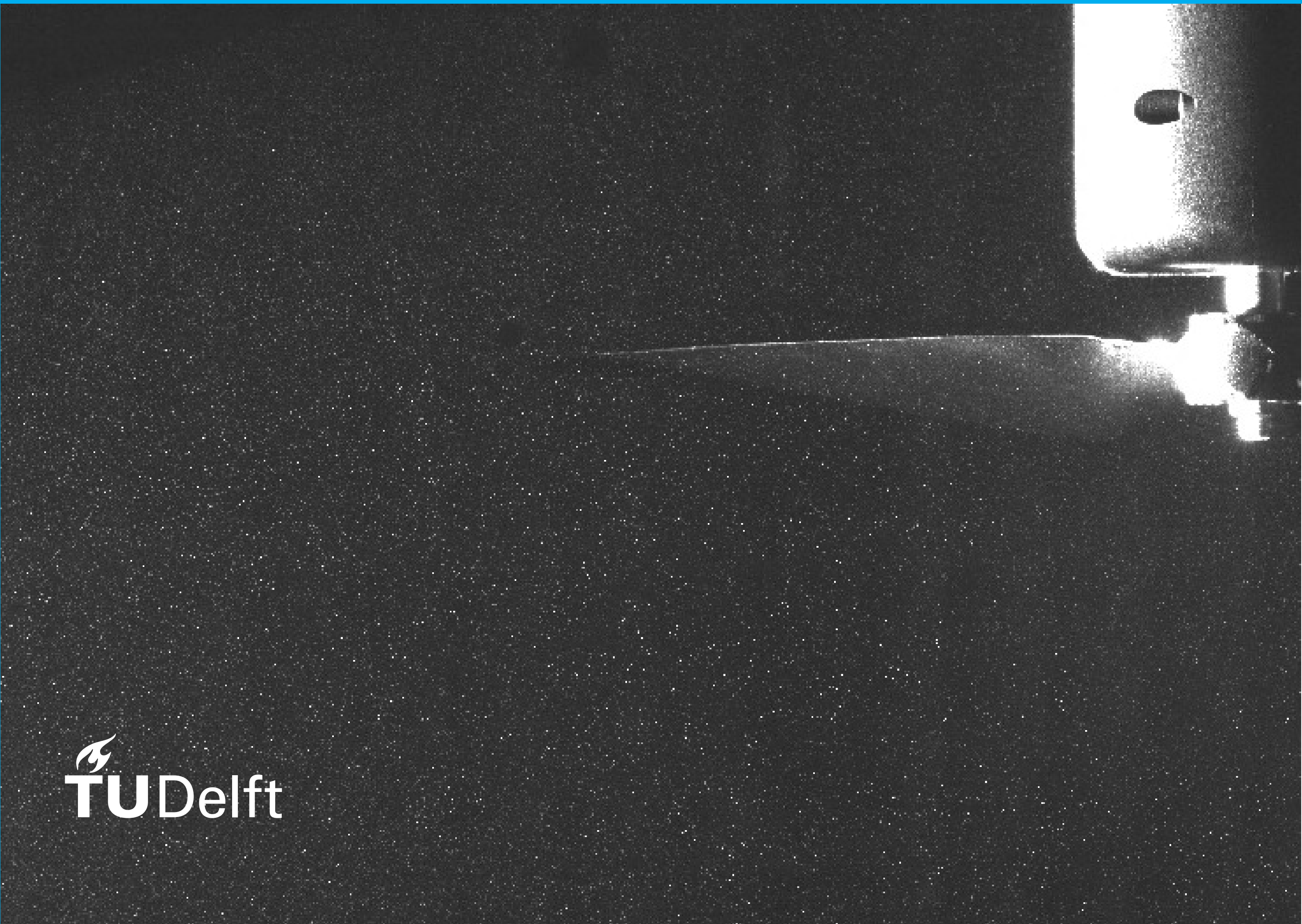

Noise radiation of a low Reynolds number propeller at an angle of attack.

An experimental and analytical study.

by

D.W. van Hoogstraten

to obtain the degree of Master of Science
at the Delft University of Technology,
to be defended publicly on Wednesday July 21, 2021 at 10:00 AM.

Student number:	4229517	
Thesis committee:	Dr. D. Ragni	TU Delft, Chair, supervisor
	Dr. F. Avallone.	TU Delft, supervisor
	E. Grande,	TU Delft, supervisor
	Dr. ir. W.J. Baars	TU Delft, external examiner

An electronic version of this thesis is available at http://repository.tudelft.nl/.

TU Delft

Abstract

This work presents an experimental and analytical investigation of unsteady loading of a low Reynolds number propeller and its relation to aeroacoustics. The propeller is positioned at an angle of attack with respect to the freestream which causes a variation in loading along the azimuth. The propeller is operated at 4000 RPM with an advance ratio of $J = 0.4$, corresponding to a free stream velocity of 8 m/s. The chord-based Reynolds number of the propeller is of the order of 10^4 and is investigated at two angles of attack: $\alpha_r = 7.5°$ and $\alpha_r = 15°$. For reference, a steady case, $\alpha_r = 0°$, is presented as well. Loading and noise measurements were carried out in the A-Tunnel of TU-Delft. Two microphone array configurations were used to mimic the observers positions *above* and *underneath* the flightpath of the propeller. Underneath the flightpath, an increase in SPL was found with increase of the rotor angle of attack. Above the flightpath, the opposite effect was observed, resulting in an asymmetrical directivity profile when the rotor is at an angle of attack. A quasi-steady loading model, based on the lifting line code Xrotor [1], is used to determine the azimuthal variation in loading. The variation in tip speed along the azimuth due to the propeller angle of attack is prescribed to determine the variation in loading in one rotation. Far-field loading and thickness noise are computed using an aeroacoustic model based on the Ffowcs-Williams & Hawkings' equation to predict the harmonic noise in the frequency domain of a rotating dipole and monopole, respectively. The numerical predictions for the steady case show good agreement for both the aerodynamic and aeroacoustic performance when compared with loading and noise measurements. For the $\alpha_r \neq 0°$ cases it was shown that unsteady loading noise increases the SPL for all harmonics, with a larger contribution at higher harmonics. When compared to the experimental spectra, the noise levels of the higher harmonics were underpredicted both above and below the flightpath.

Preface

This report presents the results and efforts invested over a period of 12 month on the understanding of the noise radiation of a low Reynolds number propeller at an angle of attack. It includes a background, based on a literature study which was delivered as a separate deliverable, a description of the experimental set-up and a description of the analytical methodology. The results of both the analytical and the experimental part are presented and discussed after which conclusions are presented.

D.W. van Hoogstraten
Delft, June 2021

Contents

List of Figures xiii

List of Tables xvii

1 Introduction 1
- 1.1 Problem Statement 1
- 1.2 Approach 2
- 1.3 Structure 2

2 Background 3
- 2.1 Different types of inflow. 3
- 2.2 Propeller Performance 3
  - 2.2.1 Reynolds number effects on propeller performance 5
- 2.3 Propeller Noise Sources 6
  - 2.3.1 Harmonic Noise 6
  - 2.3.2 Broadband noise. 7
  - 2.3.3 Airfoil Self noise 8
- 2.4 Relevance of a propeller at an angle of attack 8
  - 2.4.1 Large-scale propellers at an angle of attack 8
  - 2.4.2 Small-scale propellers at an angle of attack 12
- 2.5 Summary literature 15
- 2.6 Research goals and questions 16

3 Experimental Setup 17
- 3.1 Campaign Overview 17
- 3.2 A-tunnel 18
- 3.3 Experimental setup 18
- 3.4 Measurement Techniques. 19
  - 3.4.1 Propeller noise measurements 19
  - 3.4.2 Propeller performance measurements 19
  - 3.4.3 Oil-flow visualization 20
- 3.5 Measurement Post-Processing 21

4 Propeller performance 23
- 4.1 Zero angle of attack 23

5 Propeller Noise 25
- 5.1 Identification of different noise sources 25
  - 5.1.1 Directivity 27
- 5.2 Noise emissions from a propeller at an angle of attack 27
  - 5.2.1 Directivity 28
  - 5.2.2 Discussion 29

6 Analytical Methodology 31
- 6.1 Propeller performance prediction. 31
  - 6.1.1 Xrotor 31
  - 6.1.2 Aerodynamic section properties 32
- 6.2 Quasi-steady modelling. 34
- 6.3 Tonal noise prediction 35
  - 6.3.1 Prediction of harmonic loading noise 35
  - 6.3.2 Far-field formulation. 36

7 Synthesis 39
7.1 Steady loading . . . 39
7.1.1 Discussion . . . 40
7.2 Steady noise . . . 40
7.2.1 Remarks on the steady analysis . . . 41
7.3 Quasi-steady analysis . . . 42
7.3.1 Quasi-steady loading . . . 42
7.3.2 Discussion . . . 43
7.4 Quasi-steady loading noise . . . 43
7.4.1 Blade loading harmonics and the Bessel function . . . 43
7.4.2 Quasi-steady Noise . . . 44
7.4.3 Discussion . . . 45

8 Conclusion & Recommendations 47
8.1 Recommendations . . . 48

A Post-Processing Experimental Data 51
A.1 Data post processing routines . . . 51
A.1.1 Loadcell performance measurements . . . 51
A.1.2 Propeller noise measurements . . . 52

Bibliography 55

List of Abbreviations

AED	Automatic External Defibrilator
BEM	Blade Element Method
BL	Boundary Layer
BLH	Blade Loading Harmonic
BPF	Blade Passage Frequency
CAD	Computer-aided Design
CFD	Computational Fluid Dynamics
FWH	Ffowcs-Williams/Hawkings
LBL	Laminar Boundary Layer
NASA	National Aeronautics and Space Association
OASPL	Overall Sound Pressure Level
PSD	Power Spectral Density
RPM	Revolutions per Minute
SPL	Sound Pressure Level
TBL	Turbulent Boundary Layer
UAV	Unmanned Aerial Vehicle
UPA	Unsteady Propeller Analysis
VTOL	Vertical Take-off and Landing

Nomenclature

α	Blade section angle of attack	[°]
α_r, α_p, α_s	Angle of attack of the rotor	[°]
β	Blade twist angle	[°]
η_{prop}	Propulsive efficiency	[-]
γ	Rotor blade stagger angle	$[rad]$

Ω	Angular velocity	[rad/s]
ϕ	Observer angle around axis (spherical coordinate)	$[rad]$
ϕ'	Observer angle around axis with angular inflow (spherical coordinate)	$[rad]$
Ψ	Azimuthal position	[°]
ρ_0	Ambient air density	$[kg/m^3]$
θ	Observer angle from axis with axial inflow (spherical coordinate)	$[rad]$
θ'	Observer angle from axis with angular inflow (spherical coordinate)	$[rad]$
φ	Inflow angle	[°]
B	Number of propeller blades	[-]
c	Blade chord	[m]
c_0	Speed of sound	[m]
c_d	Sectional drag coefficient	[-]
c_l	Sectional lift coefficient	[-]
C_p	Pressure coefficient	[-]
C_T	Thrust coefficient	[-]
C_T	Torque coefficient	[-]
D	Propeller diameter	[m]
e_x, e_y, e_z	Unit vectors of main directions	$[-]$
F_s	Blade loading harmonic	$[-]$
fr	Frequency resolution	[Hz]
G	Free-space Green's function	$[-]$
J	Advance ratio	[-]
J_{mB-s}	Bessel function of the first kind of order $mB-s$	$[-]$
k_{mB}	Acoustic wavenumber	$[-]$
M	Mach number	[-]
m	BPF harmonic order	$[-]$
M_∞	Free-stream Mach number	[-]
M_{tip}	Blade-tip Mach number	[-]
n	Rotational frequency	[Hz]

p'	Acoustic pressure	[Pa]
p_{mB}	Complex acoustic pressure at a BPF harmonic	$[-]$
Q	Torque	[Nm]
R	Observer distance to origin	$[m]$
r	Radial coordinate of a source point	[m]
R'	Observer distance to source-point	$[m]$
r_{tip}	Tip radius	[m]
Re	Reynolds number	[-]
$Re_{0.75}$	Reynolds number at 0.75 of the radius	[-]
s	Loading harmonic order	$[-]$
T	Thrust	[N]
V_∞, U_∞	Freestream velocity	[m/s]
W	Effective velocity of blade element	[m/s]
W_a	Effective axial velocity of blade element	[m/s]
W_t	Effective tangential velocity of blade element	[m/s]

List of Figures

2.1 Blade section angle definition and components of the velocity triangle, adapted from [2]. 4
2.2 Lift and drag components of the blade resolved in thrust and torque components, adapted from [2]. 5
2.3 Figures retrieved from [3]. 5
  a Lift and drag coefficient of the SDA1075 airfoil for different Reynolds numbers obtained with Xfoil. 5
  b Efficiency of DA4002 propeller for different Reynolds numbers. 5
2.4 Laminar separation illustration [4]. 6
2.5 Blade angle of attack variation due to propeller angle of attack [5]. 7
2.6 Broadband noise time series example [6]. 8
2.7 Broadband noise spectrum example [6]. 8
2.8 Data obtained for chord of 22.86 cm at $\alpha = 5.4°$ for two different velocities, adapted from [7]. . . . 8
2.9 9
  a Axis of the propeller system, adapted from [8]. 9
  b Schematic of the visual and the retarded position of the propeller with respect to the observer, adapted from [9]. 9
2.10 Experimental and numerical comparison of SPL of a propeller at BPF 1, $M_a = 0.7$, $M_{tip} = 0.886$ [10]. 10
  a Prediction using steady blade surface pressure, $\alpha = 0°$. 10
  b Prediction using steady blade surface pressure, $\alpha = 3°$. 10
  c Prediction using unsteady blade surface pressure, $\alpha = 3°$. 10
2.11 Quasi-steady loading calculation and noise prediction process implemented by Zolbayar [11]. . . 11
2.12 Directivity plot of the thickness, loading and OASPL for three tip Mach numbers and two propellers of attack at an observer distance of R=30 m [11]. 12
2.13 Effect of the inclination of the propeller at cross-sectional angle of attack at different azimuthal positions [12]. 13
  a Blade cross-section at $\Psi = 90°$. 13
  b Blade cross-section at $\Psi = 270°$ 13
2.14 Unsteady loading and thrust distribution at $\alpha_s = 10°$ RPM= 6000 and $U_\infty = 20$ m/s [12]. 14
  a Unsteady loading on two small rotor blades. 14
  b Thrust distribution over the blade span at different phase angles 14
2.15 Power spectral density of the sound pressure of the propeller at $\alpha_s = 10°$, $U_\infty = 20$ m/s and $\Psi_{mic} = 0°$ [12]. 14
2.16 Comparison of SPL at different freestream velocities at RPM= 7000, $\alpha_s = 10°$ and $\Psi_{mic} = 0°$ [13]. 15
2.17 Comparison of SPL at different propeller angles of attack at RPM= 7000, $U_\infty = 15$ m/s and $\Psi_{mic} = 0°$ [13]. 15
2.18 Comparison of SPL at different freestream velocities at RPM= 7000, $\alpha_s = 10°$ and $\Psi_{mic} = 0°$ [13]. 15

3.1 Overview of the different elements of the wind tunnel experimental campaign. 17
3.2 18
  a CAD render of propeller geometry. 18
  b Propeller chord and twist distribution. 18
3.3 19
  a Propeller set-up mounted in front of the microphone array in the A-tunnel at TU-delft. . 19
  b Schematic drawing of the propeller set-up mounted in the A-tunnel. 19
3.4 Microphone positions of the microphone array, the visual position of the array corresponds to the position left of the microphone array, as depicted in Figure 3.3b. 19
3.5 Schematic representation of microphone array configuration 1 and 2. 20
  a Set-up configuration array 1. 20

b Set-up configuration array 2. 20
3.6 20
a Wyler clinotronic plus inclination sensor [14]. 20
b Schematic drawing of the loadcell with alternate cable exit [15]. 20

4.1 Bias measurements comparison at at RPM = 4000 for a range of J. 23
a Thrust coefficient corrected with bias measurements. 23
b Torque coefficient corrected with bias measurements. 23
4.2 Propeller performance over a range of J at RPM = 4000. 24
a Thrust coefficient. 24
b Torque coefficient. 24
c Propulsive efficiency. 24

5.1 Background, motor and propeller noise measured with mic_{14} at RPM = 4000, $J = 0$ with a level propeller configuration. 25
a Full spectrum. 25
b First ten BPF. 25
5.2 Background, motor and propeller noise measured with mic_{14} at RPM = 4000, $J = 0.4$ with a level propeller configuration. 26
a Full spectrum. 26
b First ten BPF. 26
5.3 Background, motor and propeller noise measured with mic_{14} at RPM = 4000, $J = 0.6$ with a level propeller configuration. 26
a Full spectrum. 26
b First ten BPF. 26
5.4 Directivity of first three BPF at RPM= 4000, $J = 0.4$ and $\alpha_r = 0°$. 27
5.5 Schematic representation of microphone array configuration 1 and 2. 27
a Setup configuration array 1. 27
b Set up configuration array 2. 27
5.6 Propeller noise measurement with array configuration 1 at RPM = 4000, $J = 0.4$ with mic_{14} and $\alpha_r = 7.5°$. 28
a Full spectrum. 28
b First 6 BPF. 28
5.7 Propeller noise measurement with array configuration 1 at RPM = 4000, $J = 0.4$ with mic_{14} and $\alpha_r = 15°$. 28
a Full spectrum. 28
b First 6 BPF. 28
5.8 Propeller noise measurement with array configuration 2 at RPM = 4000, $J = 0.4$ with mic_{14} and $\alpha_r = 7.5°$. 29
a Full spectrum. 29
b First 6 BPF. 29
5.9 Propeller noise measurement with array configuration 2 at RPM = 4000, $J = 0.4$ with mic_{14} and $\alpha_r = 15°$. 29
a Full spectrum. 29
b First 6 BPF. 29
5.10 Directivity of the SPL with array configuration 1 ($\theta = 0°$ to $180°$) and 2 ($\theta = 180°$ to $270°$) at RPM = 4000, $J = 0.4$ for different α_r. 30
a Directivity of the BPF 1. 30
b OASPL from BPF 1 to BPF 6 (110 to 820 Hz) with BPF 1.5 removed. 30
5.11 BPF 1 at different rotor pitch angles [9]. 30

6.1 Blade section angle definition and components of the velocity triangle, adapted from [2]. 31
6.2 Flowchart for calculation of the steady loading of the propeller. 32
6.3 Pressure coefficient of the airfoil independent curve and of the airfoil dependent curve plotted against free stream Mach number. 34
6.4 Blade loading modelled with the quasi-steady loading approach [16]. 34
6.5 Blade section angle definition and components of the velocity triangle, adapted from [2]. 35

6.6 System of coordinates for a single blade segment rotating dipole. 36

7.1 Oil flow visualization of the suction side of the blade at RPM= 4000 and $J = 0.4$. 39
7.2 Xrotor simulation comparison with experimental results at RPM= 4000 for different values of J. 40
  a Comparison of thrust coefficients obtained with Xrotor for different values of n_{crit}. . . . 40
  b Comparison of torque coefficients obtained with Xrotor for different values of n_{crit}. . . . 40
7.3 Noise obtained at $J = 0.4$, RPM= 4000 at a distance R of 1.5 m for BPF 1 and 2 for $\alpha_r = 0°$. 41
  a Lift, drag and thickness noise at BPF 1 compared with the experimental results. 41
  b Lift, drag and thickness noise at BPF 2 compared with the experimental results. 41
7.4 Lift, drag and thickness noise at the first 5 BPF compared to the spectrum measured with mic_{14}, $R = 1.5$ m, $fr = 1.11$ Hz. 41
7.5 Azimuthal variation of the RPM of the propeller for different values of α_r. 42
7.6 Isocontour of the sectional thrust coefficient at $J = 0.4$ and RPM= 4000 for different rotor angles of attack. 43
  a $\alpha_r = 7.5°$. 43
  b $\alpha_r = 15°$. 43
7.7 Absolute value of the BLH at $\alpha_r = 7.5°$ and $\alpha_r = 15°$. 44
  a BLH obtained at $\alpha_r = 7.5°$. 44
  b BLH obtained at $\alpha_r = 15°$. 44
7.8 Bessel function factors of steady loading noise (a) and of the first order, $s = 1$ and $s = -1$, harmonics of unsteady loading noise in (b) and (c). 44
7.9 Spectrum obtained with mic_{14} compared to the harmonics of the BPF obtained with steady and QS model at RPM= 4000, $\alpha_r = 7.5°$, $J = 0.4$ and R = 1.5 m. 45
  a Spectrum obtained with array 2 at observer angle $\theta = 90°$. 45
  b Spectrum obtained with array 1 at observer angle $\theta = 270°$. 45
7.10 Spectrum obtained with mic_{14} compared to the harmonics of the BPF obtained with steady and QS model at RPM= 4000, $\alpha_r = 15°$, $J = 0.4$ and R = 1.5 m. 45
  a Spectrum obtained with array 2 at observer angle $\theta = 90°$. 45
  b Spectrum obtained with array 1 at observer angle $\theta = 270°$. 45

List of Tables

3.1 Acquisition time for different noise measurements. 20
3.2 Operational range of loadcell and measurement uncertainty [17]. 21

4.1 Propeller performance measurement case matrix for zero propeller angle of attack and RPM = 4000. 23

6.1 Aerosection input requirements of Xrotor. 33

7.1 Thrust and torque coefficient for different values of n_{crit} compared to the experimental values at $J = 0.4$ at RPM = 4000. 40
7.2 SPL values of the steady case compared to the QS case at $\alpha_r = 7.5^\circ$ at observer positions $\theta = 90^\circ$ and $\theta = 270^\circ$. 45
7.3 SPL values of the steady case compared to the QS case at $\alpha_r = 15^\circ$ at observer positions $\theta = 90^\circ$ and $\theta = 270^\circ$. 46

1

Introduction

The term Unmanned Aerial Vehicle (UAV), or drone, refers to an automated flight vehicle. UAVs come in many different configurations, sizes and functionalities, often with vertical take-off and landing (VTOL) capabilities. They are highly manoeuvrable and versatile in the type of operation they can conduct. For example, at TU Delft a drone was designed for medical purposes, carrying an Automated External Defilibrilator (AED) and medication. In a short amount of time and with no hinder of traffic, this medical UAV can deliver emergency supplies to a nearby place. While one drone only has limited coverage, multiple drones, placed at strategical locations, can become a life saving network [18]. Another example that illustrates the wide applicability and functionality of UAVs is their deployment during natural disasters [19]. When infrastructure fails and emergency teams are unable to aid and analyse the severity of the situation, UAVs can be deployed to reach isolated areas and monitor the situation.

Although very valuable in times of emergency, this is not the only field in which drones have proven themselves useful. UAVs are widely used for military or surveillance applications, but also in agriculture, security and transportation, to give a few examples [20]. UAVs are also gaining in popularity with consumers for photography and video purposes [21][22], since the VTOL capabilities and the ability to hover have led to new perspectives and camera angles. Consumer adaptation brings the UAV more and more to the urban environment, with drones becoming more able to manoeuvre in small enclosed, urbanlike spaces, very close to people [23]. It is expected that the variety of applications of UAVs will only grow and their importance, especially in the urban environment, will increase [22][24].

While the popularity of UAVs is driven by their adaptability, functionality and their low-cost [20], their presence does not go unnoticed. In Opinion No 01/2018, published by the European Aviation Safety Agency in 2018, a noise level constraint of 60dB(A) was proposed on UAVs, measuring at 3m distance [25]. The acoustic characteristics of UAVs are therefore of great importance from an environmental and public acceptance perspective. Hence, there is a need to gain more insight in the aerodynamic and aeroacoustic performance of UAVs to reduce the noise.

1.1. Problem Statement

One of the main noise contributions of UAVs is emanated from the rotor [22] [26]. The physical mechanisms generating rotor noise were categorised by Brentner and Farrasat [27]. They identified two noise sources related to the rotation of the rotor: thickness and loading noise. Other noise sources are blade-vortex interaction noise, turbulence ingested noise, blade-self noise and high-speed impulsive noise. For UAVs equipped with small rotors, the fundamental noise generating mechanisms are the same, although not all are relevant. For example, UAVs are unlikely to generate high-speed impulsive noise as their operating tip speeds are unlikely to exceed Mach 0.3, as opposed to conventional rotorcraft for which it is not uncommon to operate at transonic tip speeds. The acoustic characteristics that small scale and larger scale helicopter rotors exhibit, have been shown to posses few similarities [28]. The difference lies to a great extent in the flow regime that they experience: the Reynolds regime that a small UAV propeller encounters is of the order of magnitude of $Re < 10^5$, while conventional manned rotor vehicles operate at a $Re > 5 \cdot 10^6$, referring to a laminar-transitional flow regime and a turbulent flow regime, respectively [22][29].

The aim of this study is to understand the effect of an angle of attack of a low Reynolds number propeller on its noise spectrum. The propeller angle of attack causes a variation in loading along the azimuth which leads to a variation in the loading noise produced by the propeller. The relevance of this is study is singular: there is a need to reduce noise of UAVs. Because of the limited operation time, it is important that UAVs can manoeuvre efficiently, completing their mission quickly and silently. This justifies the investigation of aerodynamic and acoustic performance of UAVs at different angles of inflow. In this light, a low-fidelity noise analysis method will be investigated in this thesis. To fulfil this goal the approach followed in this thesis to gain insight in the noise that is generated because of unsteady loading on a low Reynolds number fixed-pitch propeller is presented in the next paragraph.

1.2. Approach

Hypotheses and research questions are presented that act as a guide throughout this thesis. One research question focuses on an experimental approach: during a wind tunnel experiment loading and noise data is acquired by varying the propeller angle of attack for a given J. The noise is measured with a microphone array to capture the noise emitted by the propeller above and beneath the flightpath. The experiment is accompanied by an analytical model which approximates the noise using the loading data of a quasi-steady modelling scheme. A comparison is made between experimental and numerical experiment and the validity of the numerical model will be assessed.

1.3. Structure

The structure of this report is as follows. In chapter 2, first important concepts are presented after which relevant literature is discussed. At the end of the chapter the research questions are discussed. chapter 3 is the beginning of the experimental part and contains a description of the set-up. Next, the propeller performance for zero-angle of attack are presented in chapter 4, after which a description of the experimental acoustic results is presented in chapter 5. Finally, part of the analytical methodology is presented in chapter 6. In chapter 7, the analytical results are presented together with the experimental results for comparison after which the conclusions and recommendations are presented in chapter 8.

2

Background

2.1. Different types of inflow

When a UAV is operated, different flight conditions can be identified, varying from VTOL to forward flight or hover [13]. Depending on the UAV configuration, the inflow angle of the rotor changes with operation. For different configurations, such as multicopter or tilt-body, the rotor experiences different types of inflow. The rotor might encounter inflow angles varying from $\alpha_r = 0°$ up to $\alpha_r = 180°$, which are associated with axial inflow and reversed inflow, respectively [30]. The aerodynamic and aeroacoustic performance of the rotor vary for different values of α_r [9].

As an indicator for the operational state of the propeller, the advance ratio is commonly used, given in Equation 2.1. The advance ratio, J, is a non-dimensional coefficient which is defined as the ratio between the freestream velocity and the rotor tip speed. V_∞ is the incoming flow velocity in m/s, n represents the frequency at which the rotor rotates and D is the diameter of the rotor in meters [3]. In this report three different types of flow corresponding to three flight conditions are mentioned: hover, axial inflow and non-axial inflow. Hover is defined as the condition in which no freestream velocity is present. The advance ratio in this condition is zero ($J = 0$). Axial inflow describes a non-zero advance ratio state in which the freestream velocity is non-zero and aligned with the rotor axis, $J \neq 0$ and $\alpha_r = 0$. Finally, non-axial inflow describes a state in which the propeller or rotor is positioned at an angle with respect to the freestream. This state is also referred to as a propeller operating at an angle of attack, $J \neq 0$ and $\alpha_r \neq 0$.

$$J = \frac{V_\infty}{nD} \tag{2.1}$$

2.2. Propeller Performance

In order to be able to estimate the propeller performance, it is important to have a clear overview of how the propeller produces thrust. A brief description of propeller performance following from a blade element method and the corresponding coefficients is presented in this section.

A propeller is made of airfoil sections, or blade elements. In general, a propeller encounters an axial velocity, dominated by the freestream velocity, and a tangential velocity, dominated by the rotational velocity of the blade. In Figure 2.1, a schematic airfoil section of a propeller is presented with its corresponding velocity components. The effective axial velocity is denoted as W_a, the effective tangential velocity as W_t and the effective velocity seen by the airfoil section is referred to as W [2]. The induced velocities are not shown here for conciseness and an iterative approach is needed to approximate them [31].

The local angle of attack of the propeller blade section, α, is defined by the local pitch angle, β, which is given by the blade design, and the inflow angle, φ, as given in Equation 2.2. The inflow angle of each blade section can be derived from the effective tangential and axial velocity, as given by Equation 2.3.

$$\alpha = \beta - \varphi \tag{2.2}$$

$$\varphi = \arctan\left(\frac{W_a}{W_t}\right) \tag{2.3}$$

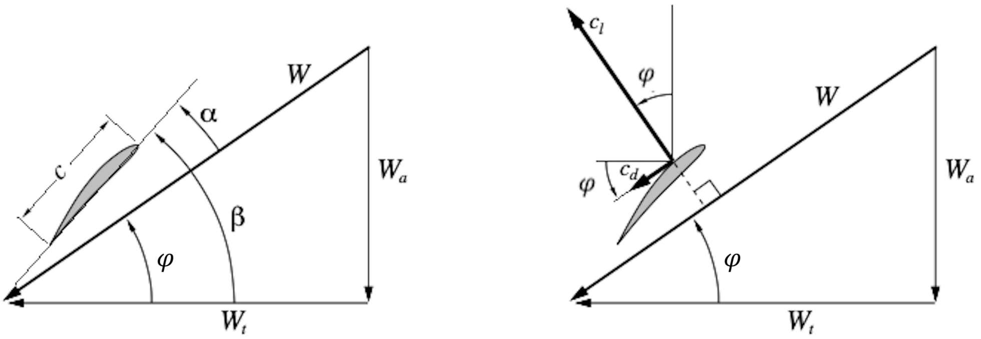

Figure 2.1: Blade section angle definition and components of the velocity triangle, adapted from [2].

Using the local angle of attack, the lift and drag coefficient of the airfoil section, c_l and c_d respectively, can be obtained. With these, the blade section lift and drag can be determined using Equation 2.4 and Equation 2.5.

$$dL = \frac{1}{2}\rho W^2 c_l c dr \tag{2.4}$$

$$dD = \frac{1}{2}\rho W^2 c_d c dr \tag{2.5}$$

The sectional lift and drag force components are then resolved into the thrust and torque. The thrust and torque produced per airfoil section is then determined by using Equation 2.6 and Equation 2.7. This is shown schematically in Figure 2.2.

$$dT = dL\, cos\varphi_i - dD\, \sin\varphi_i \tag{2.6}$$

$$dQ = (dL\, \sin\varphi_i + dD\, \cos\varphi_i) r \tag{2.7}$$

Finally, the total thrust and torque are acquired by (numerical) integration over the blade, as in Equation 2.6 and Equation 2.7.

$$T = B\int_0^R dT\, dr \approx B\sum_r dT\Delta r \tag{2.8}$$

$$Q = B\int_0^R dQ\, dr \approx B\sum_r dQ\Delta r \tag{2.9}$$

When assessing propeller performance often dimensionless coefficients are used. C_T and C_Q are the thrust and torque coefficient presented in Equation 2.10and Equation 2.11, respectively. In these equations, the variables D and n denote the propeller diameter in meters and the number of revolutions performed by the propeller per second, respectively. The fluid density is represented by ρ.

$$C_T = \frac{T}{\rho n^2 D^4} \tag{2.10}$$

$$C_Q = \frac{Q}{\rho n^2 D^5} \tag{2.11}$$

$$\eta_{prop} = J\frac{C_T}{2\pi C_Q} \tag{2.12}$$

Finally, the propeller efficiency is given in Equation 2.12 and is defined as the ratio between the power that is transferred from the propeller to the air mass moving through it and the mechanical power required to rotate the propeller [31].

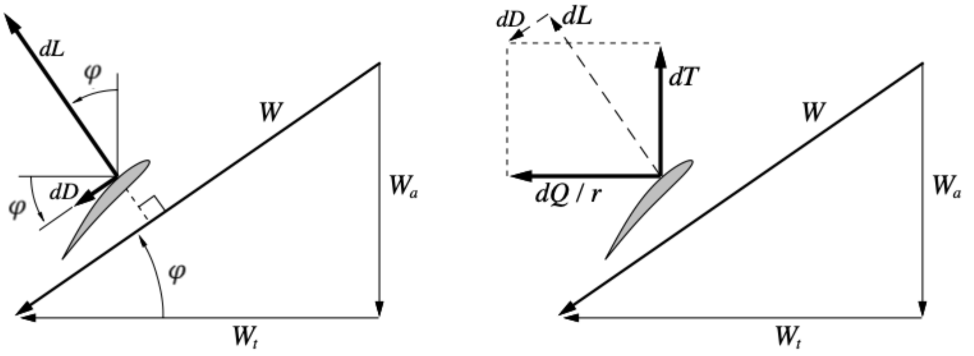

Figure 2.2: Lift and drag components of the blade resolved in thrust and torque components, adapted from [2].

2.2.1. Reynolds number effects on propeller performance

As mentioned in the introduction, Reynolds numbers lower then $100,000$ are not uncommon for small-scale propellers. The Reynolds number is defined as the ratio between viscous and inertial forces. The Reynolds number based on the chord length and velocity at the $0.75R$ radial position, where R denotes the tip radius of the rotor is represented as $Re_c = \frac{\rho_\infty \Omega 0.75 R c}{\mu_\infty}$, where ρ_∞ is the density of the ambient air, Ω is the rotational speed, c is the chord length of the blade and μ_∞ is the dynamic viscosity of air [3], [32]. The freestream velocity is assumed to be small with respect to the rotational speed and hence omitted from the equation. In this review, propellers that are referred to as *small* have a diameter of $D \leq 0.3m$ and an operational Reynolds number of $Re_c < 100,000$. Propellers that are referred to as *large* have a diameter of $D > 1m$ and operate at a Reynolds number of $Re_c > 10^6$, unless mentioned differently. This distinction is important because, in general, lift and drag are largely influenced by the Reynolds number.

In Figure 2.3a, the values of the lift and drag coefficients of a SDA1075 airfoil are plotted for different Reynolds numbers, illustrating an increase in drag and decrease in lift for lower Reynolds numbers. This means that the efficiency, as a function of both thrust and torque, is also largely dependent on the Reynolds regime in which the propeller operates, as illustrated in Figure 2.3b. The SDA1075 airfoil is used for the whole span of the DA4002 blade, except near the hub. The Reynolds number is determined by Selig et al. by the rotational velocity of the blade. When the Reynolds number is increased, a higher efficiency of the blade can be observed [3].

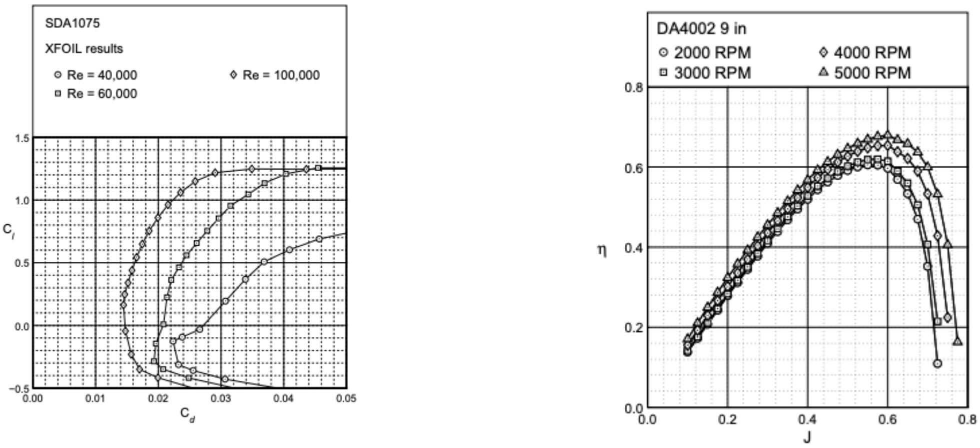

(a) Lift and drag coefficient of the SDA1075 airfoil for different Reynolds numbers obtained with Xfoil.

(b) Efficiency of DA4002 propeller for different Reynolds numbers.

Figure 2.3: Figures retrieved from [3].

Because the behaviour of the boundary layer (BL) changes with Reynolds number in terms of flow separation, amount of laminar/turbulent flow and reattachment zones for example, the lift and drag change as well [32]. At low Reynolds numbers a laminar separation bubble may develop on the airfoil. In Figure 2.4, a schematic representation of the development of a laminar separation bubble is presented. At point *S*, an adverse pressure gradient forces the laminar flow to separate from the airfoil. A transition point can be identified at point *T*, where the separated flow transitions to turbulent. The turbulent flow re-energises from the freestream and reattaches to the airfoil at point *R*. After point *R*, generally a turbulent boundary layer (TBL) continues downstream. The TBL is less susceptible to separation because it is re-energised by the free stream and hence remains attached to the airfoil. As the angle of attack is increased, the TBL will eventually separate close to the trailing edge. Separation will lead to an increase in drag and a decrease in lift. When the angle of attack is further increased, the separation point will move upstream over the airfoil towards the leading edge and eventually stall will occur [32].

The size of the separation bubble has an influence on the lift and drag that an airfoil produces. When the Reynolds number is decreased from 100,000 to 50,000, the thickness of the TBL and the separation bubble both increase in dimension [32]. According to Selig et al., a decrease in Reynolds number will generally lead to an increase in the size of the separation bubble [3]. As a consequence, the airfoil will experience a decrease in lift and an increase in drag. As the Reynolds number represents the ratio between viscous and inertial forces, the contribution of the viscous forces can be said to be higher in this regime. Between Reynolds numbers from 10.000 to 50.000, the reattachment point lies relatively close to the trailing edge even at low angles of attack. If the angle of attack is increased, the reattachment point moves further towards the leading edge, creating a large separation zone [32].

In their research, Selig et al. pose a few hypotheses: the lift coefficient decreases and the drag coefficient increases when the Reynolds number decreases. Consequently, the thrust coefficient decreases or the power coefficient increases, or both occur at the same time. These hypotheses were verified by Selig et al. and an increase in propeller efficiency was observed when the Reynolds number increases. Selig et al. note that, despite the efficiency increase with increase in Reynolds number, the efficiency is still low when compared to a full scale propeller [3].

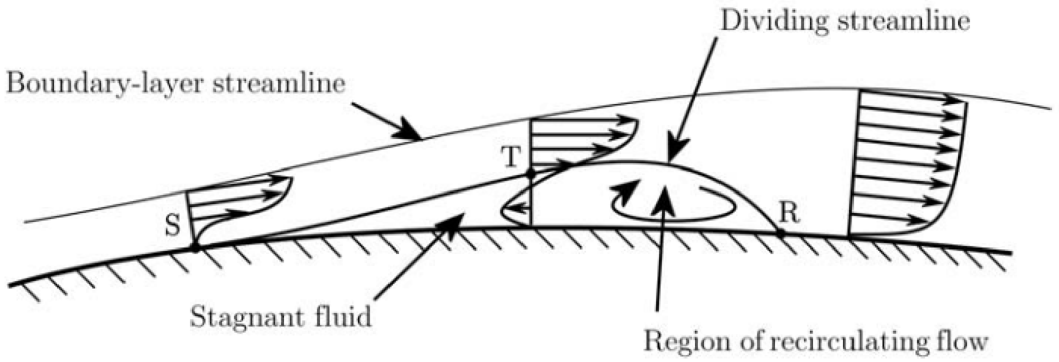

Figure 2.4: Laminar separation illustration [4].

2.3. Propeller Noise Sources

The noise generation mechanisms are similar for all rotors and propellers. The dominant mechanisms, however, depend on size and operating Reynolds regime. When considering different types of noise of propellers in general, a distinction is made between harmonic or tonal noise and broadband noise [33].

2.3.1. Harmonic Noise

Harmonic or tonal noise is related to the periodic motion of a propeller. When assuming an ideal propeller, harmonic noise can be identified at the harmonics of the Blade Passage Frequency (BPF), which is defined as the rotational frequency multiplied with the number of blades, given in Equation 2.13.

$$n \cdot \mathrm{BPF} = n \cdot B \frac{\mathrm{RPM}}{60} \tag{2.13}$$

In this equation *B* is the amount of blades of the propeller. Multiple harmonic tones appear at multiples of the BPF. The multiples of the BPF are indicated by the n in Equation 2.13, where $n > 0$.

Propeller noise calculations are often derived from a solution of the Ffowcs-Williams and Hawkings equation (FWH) [34]. The FWH acoustic analogy decouples the propagation of the noise from its sound generating mechanisms. This is done by reformulating the exact Navier-Stokes and continuity equation in the form of a inhomogeneous wave equation. The different noise source mechanisms appear as source terms of the wave equation [35].

The mechanisms that contribute to harmonic noise are related to a thickness source term, a loading source term and a quadrupole source term. The quadrupole term has been shown to be only important in transonic Mach regimes [36]. Consequently, if the propeller has thin blades and operates in the subsonic Mach regime, the quadrupole term of the equation can be neglected. Thickness noise is a result of the fluid displacement by the volume of the propeller blades, and can be described by a moving monopole [27]. The loading counterpart is responsible for the steady and unsteady loading on the blade [37]. Loading noise is generated by the pressure field around the blades, that generates forces: lift and drag. As the blade moves through the air, it exerts these forces on the medium and hence creating pressure fluctuations from an observer point of view. The noise of a moving force can be described by the radiation of a moving dipole [38].

When a non-axial inflow is introduced to the propeller, a constant change in loading over the azimuth is observed for the blade. This change in loading over the azimuth is the result of a varying magnitude of the velocity of the blade per azimuthal position. The in-plane velocity component, V_z, is, depending on the azimuthal position of the blade, subtracted or added to the rotational velocity. In Figure 2.5, it can be observed that when the blade is going up, the angle of attack of the blade section is smaller than when the blade is going down, due to change in velocity with azimuthal position. As a consequence, the propeller experiences asymmetric loading.

The thickness and loading pressure fluctuations are often calculated using Formulation 1A, expressed by Farassat, of the FWH equation. The sum of the thickness and loading pressure gives the acoustic pressure contribution to harmonic noise and can be written as [38][39]:

$$p'(\mathbf{x},t) = p'_T(\mathbf{x},t) + p'_L(\mathbf{x},t) \tag{2.14}$$

Where the acoustic pressure is given by p', $\boldsymbol{x}$ represents the observer position and the observer time is t.

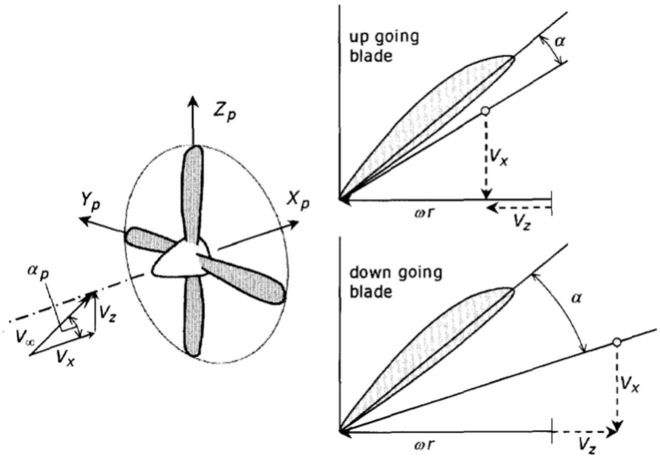

Figure 2.5: Blade angle of attack variation due to propeller angle of attack [5].

2.3.2. Broadband noise

Broadband noise is related to the interaction of the blade with turbulent flow structures. In general, this noise is shed at the interaction of the turbulent flow with the leading edge or the trailing edge [40]. It differs from harmonic noise in the sense that it is random in nature: it is emitted at different amplitudes over a wide range of frequencies [6]. An example of the amplitude of a broadband signal is given in Figure 2.6. Its spectrum is presented in Figure 2.7. For propellers, the contribution of broadband noise to the overall sound pressure level (OASPL) is regularly of less importance than the tonal contribution. Furthermore, a contribution to the

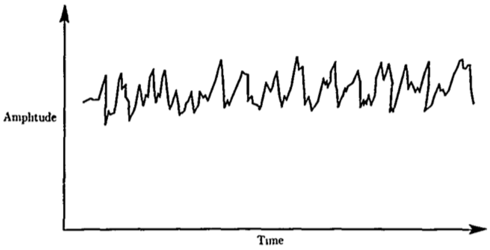

Figure 2.6: Broadband noise time series example [6].

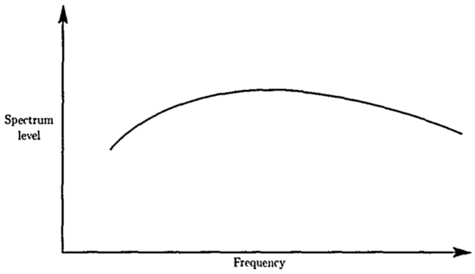

Figure 2.7: Broadband noise spectrum example [6].

broadband noise can be attributed to the possibility of flow separation [41]. The broadband spectra can then be defined as the sum of these parts, as presented in Equation 2.15.

$$p'_{BB} = p'_{TE} + p'_{LE} + p'_{S} \tag{2.15}$$

where, p'_{TE}, corresponds to the trailing edge component, p'_{LE}, to the leading edge component and p'_{S}, to the flow separation component [42]. An illustration in which the contribution of flow separation noise and TBL trailing edge noise can be identified is presented in Figure 2.8. Flow separation contributes to the hump like shape of the broadband noise.

2.3.3. Airfoil Self noise

In the laminar-transitional flow regime, two types of noise can be generated by the interaction with the BL. The noise that is generated by a laminar boundary layer (LBL) differs distinctly from that generated by a TBL. According to Yakhina et al. [43], a LBL is a necessary but not a sufficient condition for the generation of tonal noise. To generate high-amplitude tones, a combination of a very thin separation bubble with an unstable BL and an acoustic feedback loop are required. The noise is generated from the laminar separation bubble due to scattering of a coherent structure at the trailing edge [44]. It is shown by Yakhina et al. that this mechanism can be present in rotating blades. When the flow has transitioned, a TBL flows over the trailing edge of the airfoil. The noise created by the interaction of the TBL and the trailing edge is affected by the location of transition as this determines the BL thickness at the trailing edge. Where noise generated by the LBL is quasi-tonal, the noise generated by the TBL can be classified as broadband.

2.4. Relevance of a propeller at an angle of attack

In this section, first several research papers with respect to large rotors, at an angle of attack are presented. Afterwards, a small UAV multicopter rotor in forward flight is investigated in terms of loading and noise.

2.4.1. Large-scale propellers at an angle of attack

In the 80's and 90's endeavours were undertaken by the National Aeronautics and Space Association (NASA) to capture the effect of a propeller angle of attack with respect to the freestream on its acoustic spectrum.

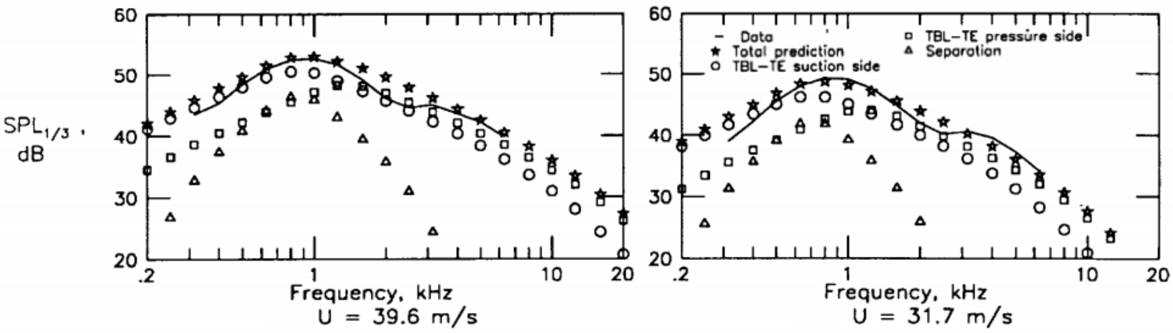

Figure 2.8: Data obtained for chord of 22.86 cm at $\alpha = 5.4°$ for two different velocities, adapted from [7].

Five research papers are discussed in this subsection, of which the first four are by NASA and the last one is a more recent endeavour.

To gain more insight in unsteady loading introduced by an angle of attack of a propeller, Takallu and Lessard investigated the periodic aerodynamic loads produced by an advanced turboprop propeller [8]. The propeller used for the simulations was the $SR-7L$, measuring a 1.37 m in diameter and counting eight blades. The simulations were run for propeller angles of attack ranging from $\alpha_r = -3^\circ$ to $\alpha_r = 5^\circ$. The orientation of the blade is given in Figure 2.9a. The forward velocity is given by V_0 and V denotes the velocity seen by the propeller. The propeller angle of attack is represented in the figure by α_p and ω is the rotational velocity.

For the advancing blade that moves downward at $\Psi = 0^\circ$, a larger velocity was observed when compared to the retreating blade, moving upward at $\Psi = 180^\circ$, at a positive angle of attack of the propeller. Furthermore, the computed flow separation region that was observed for the $\Psi = 0^\circ$ position was smaller than at the $\Psi = 180^\circ$. This is reversed when the angle of attack of the propeller changes sign by tilting the propeller downward. Although expected, the radial distribution of the blade section angle of attack increases when the propeller inclination angle is increased, implying larger dynamic variations in instantaneous blade loads. Takallu and Lessard conclude that, although the time averaged blade performance is not much affected by the incidence angle of the propeller, the dynamic variations of the blade loading are large.

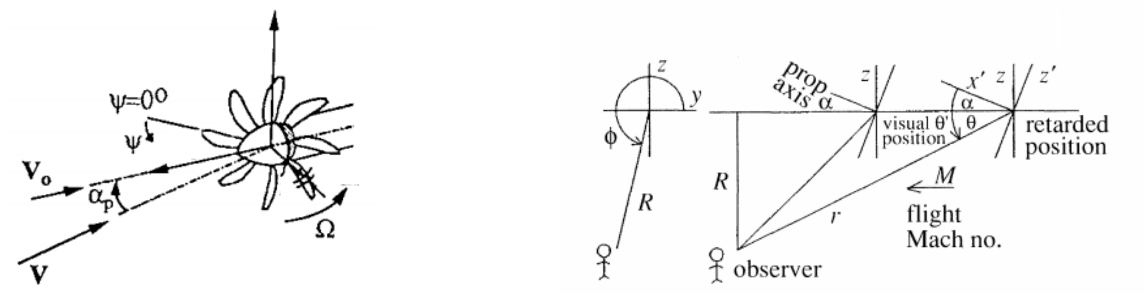

(a) Axis of the propeller system, adapted from [8].

(b) Schematic of the visual and the retarded position of the propeller with respect to the observer, adapted from [9].

Figure 2.9

The results presented by Takallu and Lessard illustrate what the effect of an angle of attack of the propeller on the blade loading can be. Although it was not investigated by Takallu and Lessard, the large variation in loading of the blade with its phase angle will almost certainly impact the radiated noise by the blade.

A theoretical investigation of the sound of a propeller at an angle of attack was performed by Hanson [9]. Hanson derived that the angular inflow of a propeller may result in two effects: first, the angle of attack seen by the blade sections varies along the azimuth and leads to unsteady blade loading. Second, he found that the radiation efficiency under the flight path of the propeller ($\phi = 270^\circ$, Figure 2.9b) was increased. The tilt of the propeller increases the Mach number of the blade section relative to the observer and increases the efficiency of noise radiation, leading to higher noise levels below the propeller. This effect is called differently throughout literature, in this review the term "velocity effect" is adopted. In Figure 2.9b, θ is the angle between the flight direction and the observer and α is the propeller angle of attack. The azimuth angle is denoted by ϕ. The vector $\boldsymbol{r}$ denotes the distance between the propeller centre at the location of emission to the observer. A prime indicates the axis of the tilted system.

It is shown by Hanson that the Doppler factor, given by $1 - M \cos\theta$, varies with ϕ', which is the propeller azimuth angle when the propeller is at an angle of attack. When $\alpha > 0$ and the position of the observer is underneath the propeller at $\phi' = 270^\circ$, $\cos\theta$ increases and thereupon, the convective amplification factor, denoted by $1/(1-M\cos\theta)$, increases. To summarise, the change in velocity of the propeller along the azimuth causes a change in Doppler amplification. Consequently, there is a noticeable difference between the noise radiated below the propeller at $\phi = 270^\circ$ and above the propeller, $\phi = 90^\circ$.

The Mach numbers investigated by Hanson for a $4m$ diameter propeller are $M = 0.2$ and $M = 0.8$. The propeller angles of attack range from $\alpha = 0^\circ$ to $\alpha = 15^\circ$ for the $M = 0.2$ case and from $\alpha = 0^\circ$ to $\alpha = 5^\circ$ for the $M = 0.8$ case. Hanson concludes with the remarks that at the BPF, unsteady loading and the velocity effect, due to the angle of the shaft, equally affect the noise increase.

In another investigation that Hanson conducted together with Parzych, similar observations were found.

Hanson and Parzych investigated how the harmonic noise is affected by angular inflow, both numerically and experimentally [45]. They developed a frequency domain theory for the radiation of propeller harmonic noise when subjected to angular inflow. The theory is based on Goldstein's acoustic analogy [46]. The theory developed by Hanson and Parzych is exact, in the sense that if the aerodynamic data and the geometry given are correct, the noise predictions will also be correct. The resulting programme was called WOBBLE and follows the notation of the report closely. The authors note that the theory is only applicable to angular inflow and not distorted inflow. Hanson and Parzych observed two effects: an unsteady loading effect and an unsteady velocity effect which affects both loading and thickness noise.

To demonstrate the influence of the blade loading on the predicted noise, the loading was determined using a lifting line method and used as input for the noise prediction. The results were compared with experiments of propeller and prop-fan data. The propeller had a diameter of 2.03 m and the inflow angle ranged from −7.4° to +7.3°. The prop-fan had a diameter of 2.74 m and the inflow angles ranged from −10° to 15°. The respective operational Mach numbers were 0.15 and 0.8. Where the inclusion of the unsteady loading and the velocity effect showed good agreement with the propeller data over the range of inflow angles up until the fifth harmonic, the prop-fan comparison was not so good. Hanson and Parzych believed that this was due to poor aerodynamic data.

What can be taken from this investigation is that the harmonic acoustic part can be modelled accurately: when the aerodynamic data is correct, the noise generation output is correct. As indicated, Hanson and Parzych endeavoured to derive a theory for propeller harmonic noise and hence the broadband contribution is not investigated. Therefore it remains uncertain how the broadband component of the noise is affected by the propeller angle of attack.

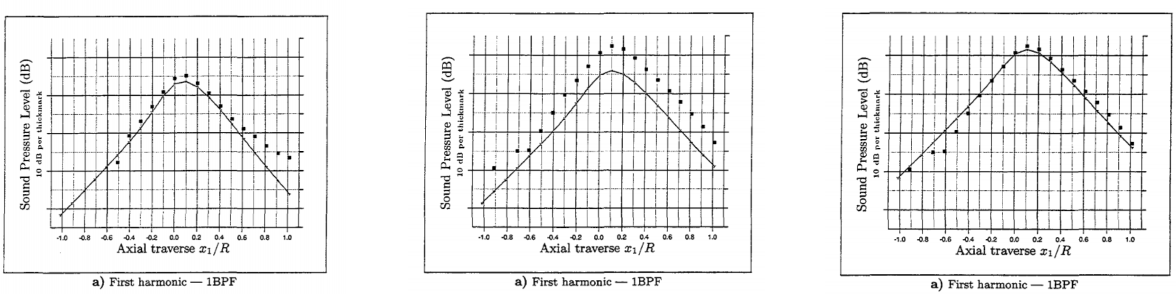

(a) Prediction using steady blade surface pressure, $\alpha = 0°$.

(b) Prediction using steady blade surface pressure, $\alpha = 3°$.

(c) Prediction using unsteady blade surface pressure, $\alpha = 3°$.

Figure 2.10: Experimental and numerical comparison of SPL of a propeller at BPF 1, $M_a = 0.7$, $M_{tip} = 0.886$ [10].

Another investigation, in which the noise of a subsonic propeller at a propeller angle of attack was explored, was performed by Frota, Lempereur and Roger [10]. Their findings agreed with the earlier findings of Hanson and Parzych: due to the incidence angle of the rotor the blade loading becomes unsteady and affects the noise. According to the authors, the change in angle of attack has a double effect on the noise generation: mostly this due to unsteady loading, but, as mentioned by Hanson [9], there is also a velocity effect. The velocity effect amplifies the noise underneath the propeller.

They tried to capture the effects of a propeller angle of attack on the noise numerically and to validate their findings with experiments. Their results are presented partly in Figure 2.10. The dataset used for their noise calculations was obtained after interpolation of the test data from pressure transducers that measured the pressure fluctuations at the blade surface. For the noise prediction a code named $BRAVHA$ was used which encorporates the time domain Formulation 1A of the FWH. In Figure 2.10, the experimental values are represented by dots and the line corresponds to the numerical analysis. Note that in Figure 2.10a and Figure 2.10b, a steady numerical model is used, as compared to Figure 2.10c, in which an unsteady module is included.

The velocity effect can be identified when Figure 2.10a and Figure 2.10b are compared. Both numerical noise calculations use the steady blade surface pressure, excluding the unsteady loading noise contribution. An increase in the numerical noise for all microphone positions can be identified for the $\alpha_r = 3°$ case when compared to the $\alpha_r = 0°$ case. When the numerical results are inspected a difference of 2 to 3 dB can be observed. When the unsteady module is enabled, the numerical analysis in Figure 2.10c gives a better approximation to the experimental data than the steady analysis, presented in Figure 2.10b. Furthermore, when the angle of attack of the propeller is changed from 0° to 3° (Figure 2.10a and Figure 2.10b respectively), an increase in perceived noise is observed for the experimental data varying between 5 and $7dB$. Note that this increase in noise is both due to the unsteady loading and the velocity effect.

Only a small difference in angle of attack can make a large impact on the sound level produced by a propeller. Furthermore, the increase in unsteady loading is an important aspect of the noise signature which, when left out, can lead to severe underestimation of the noise. It is important to state that Frota, Lempereur and Roger only explored the influence of the angle of attack on the first 3 BPF. The higher harmonics and the broadband component of the noise are omitted in this research.

Finally, a more recent investigation considering the noise of a low speed large propeller is performed by Zolbayar [11]. In his thesis he explores the harmonic noise characteristics of isolated propellers which are designed to operate at a tip speed of $M_{tip} = 0.3$ and $M_{tip} = 0.4$. The propellers have a diameter of $2.1m$. In designing the rotors, the forward speed, thrust and radius are fixed at 51.44 m/s, 1.05 m and 2800 N for all rotors. The number of blades is given as input and the chord distribution is then given as design output. It is noted that the chord distribution is not presented by Zolbayar and hence no approximation of the Reynolds number can be made. The propellers were designed in CROTOR, which uses a blade element method combined with a minimum induced loss routine [2]. Furthermore, the two designed propellers were compared to a three bladed propeller with a tip speed of $M_{tip} = 0.7$. The noise of the propellers was evaluated at an angle of attack of $\alpha_r = 0°$ and $\alpha_r = 10°$.

To model the unsteady loading, introduced by the angle of attack of the propeller, Zolbayar adopted a quasi-steady modelling approach. Zolbayar determined the velocity of the rotor tip at 30 different positions along the azimuth. For each of these positions, the steady loading was calculated using the previously determined tip speed. CROTOR outputs the lift and drag coefficients for each azimuthal position, which then have to be made dimensional for the input in PSU-WOPWOP. A schematic illustration of the quasi-steady modelling approach is presented in Figure 2.11.

The results obtained with the quasi-steady modelling approach agree with the earlier findings by Hanson and Parzych, in the sense that an unsteady loading effect and a velocity effect can be observed. As can be seen in Figure 2.12, an increase in noise underneath the flightpath of the propeller can be observed. It is noticed by Zolbayar that the unsteady loading becomes more dominant at lower tip speeds, as the thickness noise component appears to diminish quicker with tip Mach number than the loading noise component. Furthermore, a slight decrease in the noise levels above the rotor (90°) can be observed for the propeller angle of attack case when compared to the zero angle of attack case.

The quasi-steady modelling method introduced by Zolbayar seems very interesting in the sense that, with low degree of complexity, an approximation can be made of the unsteady loading of the propeller and its noise. The quasi-steady modelling approach seems to correspond with the unsteady loading and velocity effects found earlier. It is noted that the blades of the propellers are still large compared to a small UAV propeller.

Some remarks are in order with respect to the model: it is not validated and the study was purely numerical. Also, the broadband component of the noise spectrum was not taken into account. Furthermore, only the OASPL was presented and no frequency spectrum was evaluated. The quasi-steady modelling approach does not consider the possible interaction effects of the different azimuthal positions. Therefore, although

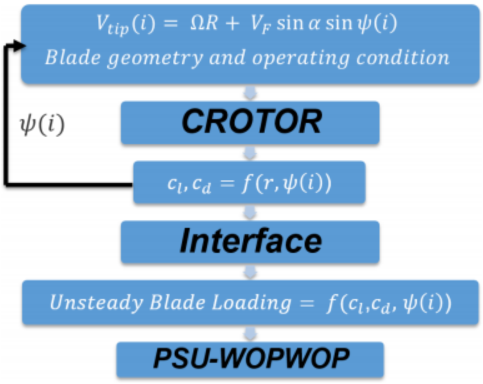
$V_{tip}(i) = \Omega R + V_F \sin\alpha \sin\psi(i)$
Blade geometry and operating condition
$\psi(i)$
CROTOR
$c_l, c_d = f(r, \psi(i))$
Interface
Unsteady Blade Loading = $f(c_l, c_d, \psi(i))$
PSU-WOPWOP

Figure 2.11: Quasi-steady loading calculation and noise prediction process implemented by Zolbayar [11].

the modelling of the unsteady loading with this quasi-steady modelling method seems promising, a lot of uncertainties still remain with respect to how the noise calculations would compare to experimental results.

In summary, it has been shown how an angle of attack influences the dynamic loading of the blade. The effects of angular inflow on its acoustic spectrum were observed by Hanson and Parzych and Frota, Lempereur and Roger [10], [45]. Although the data fed into their acoustic prediction models differed, their conclusions about the effect of the angular position of the propeller with respect to the freestream were similar. Two main causes for the increase in noise were found, as stated later by Hanson [9]: first, the unsteady loading and second, the increase in Mach number of the blade with respect to the observer. It was observed that no full spectral analysis was performed in these studies, as only the first harmonics were investigated. Furthermore, a quasi-steady modelling approach was introduced which combined a steady blade element method with a variation of the tip-speed along the azimuth, resulting in a quasi-steady approximation of the unsteady loading of the propeller. This method was found to approximate the unsteady effects introduced by the propeller angle of attack well.

Overall, a clear increase in SPL of the harmonic component can be observed with a small increase in angle of attack but no general, quantitative rule is derived. As mentioned before, although the same principles with respect to noise generating mechanisms apply, a one-to-one comparison cannot be made because the propellers from the mentioned studies and small UAV propellers, operate in different Reynolds regimes. From the findings in this section, it has become clear that the harmonic noise of a small propeller will be affected by an increase in propeller angle of attack. However, it remains uncertain how much the unsteady loading and velocity effect will contribute. Furthermore, the influence of the propeller angle of attack on the broadband component remains unknown.

2.4.2. Small-scale propellers at an angle of attack

Non-axial inflow occurs mainly in forward flight and transitioning from one operation phase to another. In this section two papers discussing a multicopter propeller in forward flight are presented.

Experimental and numerical analyses were performed by Yang et al. to quantify the aerodynamic char-

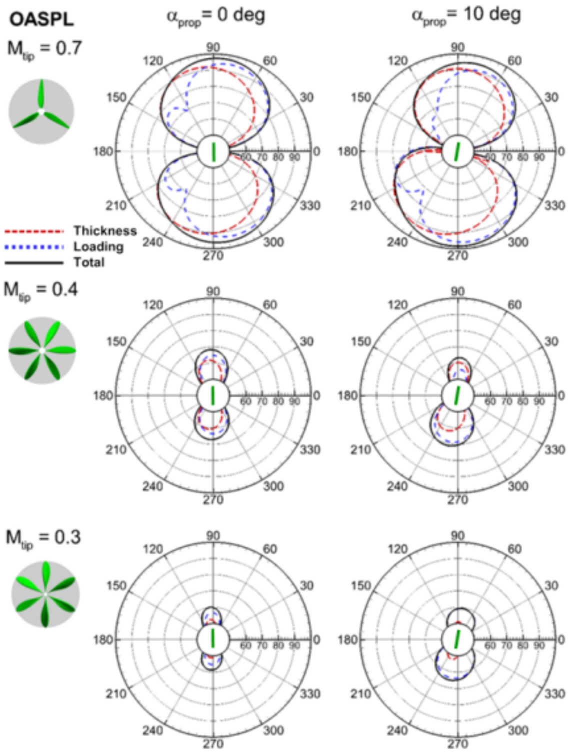

Figure 2.12: Directivity plot of the thickness, loading and OASPL for three tip Mach numbers and two propellers of attack at an observer distance of R=30 m [11].

acteristics of a multicopter propeller while operating in forward flight [12]. The aeroacoustic characteristics were determined experimentally. The rotor used in the experiment had two blades and a diameter of 0.206 m. The tests were conducted in an anechoic wind tunnel with a turbulence level of 0.05%. The propeller was attached to a strut with a pivot enabling Yang et al. to adjust the angle of attack. For the numerical counterpart of the experiment, a similar turbulence level was used in a CFD analysis. The Reynolds number was set to $5.6 \cdot 10^4$ at the blade tip. The turbulence model that they used was the $k-\omega$ model. The authors note that although a fully turbulent simulation of the flow is not ideal for the Reynolds number used in this experiment, the findings correspond well to the experimental results. Only one simulation was performed at 6000 RPM while the experiment was conducted for multiple rotational speeds.

The blade loading of the propeller is dependant on its circumferential position, denoted as the phase angle, Ψ. In Figure 2.13a, the relative circumferential position of the blade and its corresponding angle of attack are presented. The angle of attack is defined as the angle between the resultant velocity, U_{Re}, and the chord line of the blade section. The resultant velocity is the sum of the axial velocity vector and the tangential velocity vector seen by the blade section. The axial velocity vector is the summation of the freestream component in direction of the propeller axis and the induced axial velocity. The summation of the rotational speed, the in-plane component of the freestream velocity and the induced tangential velocity represent the tangential velocity. When Figure 2.13a is compared to Figure 2.13b, it can be observed that the angle of attack is larger at $\Psi = 90°$ than at $\Psi = 270°$. This is due to the X-component of the free stream velocity, $U_\infty \cos(\alpha_s)$, which has an increasing effect on the resultant velocity of the blade section at $\Psi = 90°$ and a decreasing effect on the resultant velocity of the blade section at $\Psi = 270°$, correspondingly increasing and decreasing their respective angle of attack.

The thrust coefficient of two individual blades and the overall system is presented in Figure 2.14a. This graph illustrates the dynamic loading of the individual blades and the propeller at different phase angles. At $\Psi = 105°$, the maximum thrust value of blade 1 occurs, while at $\Psi = 264°$ the minimum thrust value is identified. The difference between these values is not 180°, as one might expect. This is probably because of the asymmetric slipstream. The authors note that consequently the induced velocity is not symmetric either. The phase angles at which the maximum and minimum value of thrust occur can be said to be a function of the propeller angle of attack as well and may differ accordingly.

In Figure 2.14b, the thrust per blade at different phase angles is presented. The red lines in the graph correspond to the advancing blade, the black lines correspond to the retreating blade. It becomes immediately clear that the thrust produced by a single blade of the propeller is very much dependant on the phase angle of that blade. It can be observed that the highest thrust happens at $\Psi = 90°$ and a negative thrust can be observed for the inboard part of the blade at phase angles $\Psi = 225°, 270°$ and $315°$. It is also observed that for the retreating blade, the decay of the thrust near the tip is less pronounced.

Futhermore, Yang et al. researched the pressure coefficient at $0.75R$ for similar blade angles, Ψ, as found in Figure 2.14b. They observed a separation bubble at $\Psi = 135°$. It is not known if flow separation occurred at other radial locations, leading to additional disturbances. In this configuration, where the tip vortex is convected in plane of the rotor, the risk of blade-vortex interaction is higher than for close-to-axial inflow angles. This because in the latter case, the tip vortices are convected out of plane. If and where blade-vortex interaction might occur for close-to-axial inflow, remains a topic for speculation but will surely depend on the freestream velocity and the propeller angle of attack.

In Figure 2.15, the PSD of the sound pressure of the propeller at $\alpha_s = 10°$, $U_\infty = 20$ m/s and $\Psi_{mic} = 0°$ is presented. What can be observed is that maximum value of the PSD is at BPF 1 as expected. BPF 7

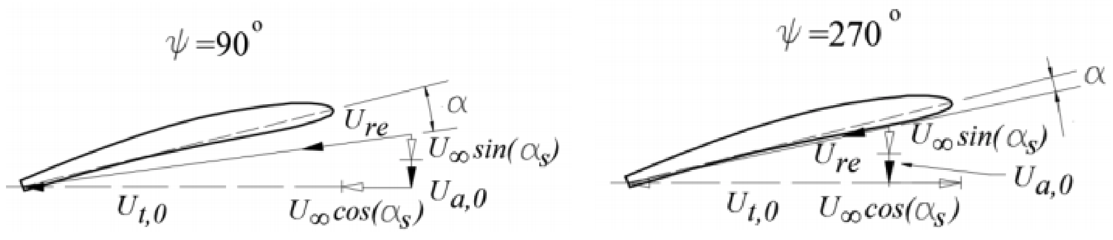

(a) Blade cross-section at $\Psi = 90°$.

(b) Blade cross-section at $\Psi = 270°$.

Figure 2.13: Effect of the inclination of the propeller at cross-sectional angle of attack at different azimuthal positions [12].

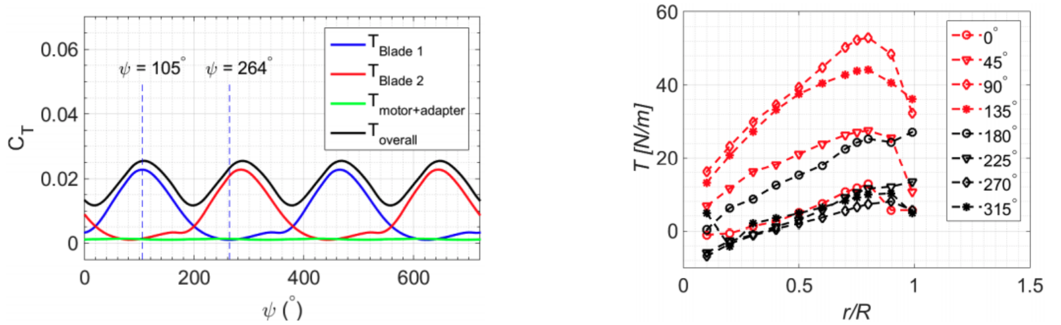

(a) Unsteady loading on two small rotor blades.

(b) Thrust distribution over the blade span at different phase angles

Figure 2.14: Unsteady loading and thrust distribution at $\alpha_s = 10°$ RPM= 6000 and $U_\infty = 20$ m/s [12].

corresponds with the polar number of the electric motor. The motor is assumed to give the main contribution to the peak at BPF 7. Furthermore, what is interesting is that the tonal peaks seem to remain up until a frequency of about 3500 Hz, corresponding to BPF 21 at 5000 RPM. Although lower in magnitude than BPF 1, distinctive tones can still be noticed. This differs from the static and axial flow cases investigated earlier. This is unmentioned by the authors and is probably due to the unsteady loading that affects the mid frequencies [47].

The asymmetric inflow causes unsteady loading which influences the noise characteristics of the propeller. It was observed that, as the advance ratio decreased, the SPL of BPF 1 increased. The OASPL directivity followed the same directivity as that of the SPL at BPF 1 and hence it was concluded that the tonal noise is the more dominant noise source for this propeller. Similar to what was observed by Marino, the SPL increases when the advance ratio decreases.

Some comments can be made about the numerical analysis of Yang et al. as no noise analysis was performed with the CFD results. The CFD results showed promising similarities with the experiments in terms of capturing the dynamic thrust coefficient.

Yang et al. further explored the forward flight of a multicopter propeller by investigating the full performance of a full-scale isolated rotor [13]. In this experiment, the same test-setup was used as in the previous experiment [12]. They observed that when the freestream velocity increases, the tonal as well as the broadband noise increase, for a constant RPM and propeller angle of attack, as presented in Figure 2.16. The authors note that the increased broadband noise might be because of increased wind tunnel jet velocities. When the freestream velocity is increased, the axial component of the velocity increases and has a decreasing effect on the thrust due to the decreased angle of attack of the cross section of the blade. Furthermore, the in-plane component of the velocity has an effect on the incoming flow which varies with the phase angle Ψ. It increases the thrust on the blade in the first two quadrants and reduces the thrust in the third and fourth quadrant.

A similar analogy can be made for a constant RPM and freestream velocity, as the thrust decreases due to an increase in propeller angle of attack. This is because when the propeller angle of attack increases, the axial component, $U_\infty \sin(\alpha_s)$, increases. The angle of attack of the blade cross section is then reduced due to the increased axial velocity component. Simultaneously, the angle of attack is decreased due to the in-plane velocity component, which decreases when the propeller angle of attack increases. It can be observed in

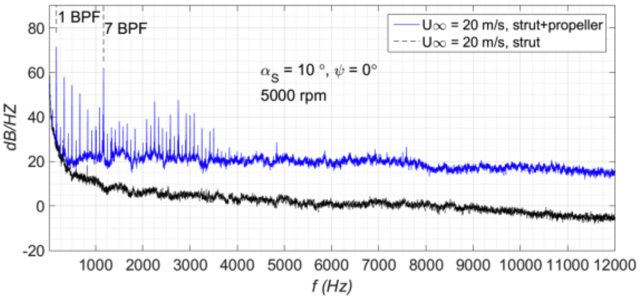

Figure 2.15: Power spectral density of the sound pressure of the propeller at $\alpha_s = 10°$, $U_\infty = 20$ m/s and $\Psi_{mic} = 0°$ [12].

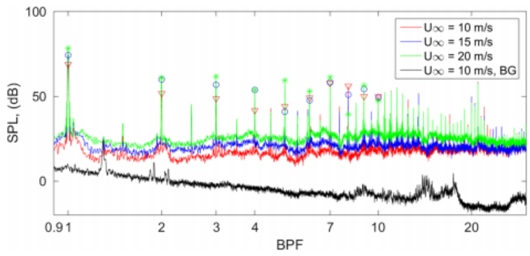

Figure 2.16: Comparison of SPL at different freestream velocities at RPM= 7000, $\alpha_s = 10°$ and $\Psi_{mic} = 0°$ [13].

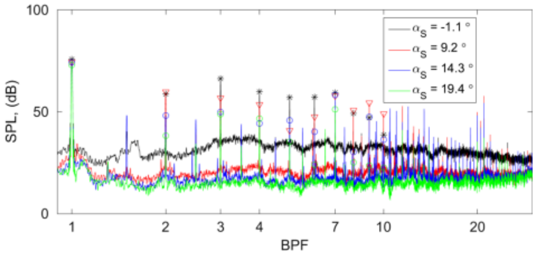

Figure 2.17: Comparison of SPL at different propeller angles of attack at RPM= 7000, $U_\infty = 15$ m/s and $\Psi_{mic} = 0°$ [13].

Figure 2.17, that for an increasing angle the SPL decreases. The SPL at BPF 1 and the OASPL are presented in Figure 2.18. As the freestream velocity increases, the SPL increases for both figures. This seems logical as the difference in velocity between the retreating and the advancing blade increases when the velocity increases. The noise then, increases accordingly. Furthermore, the OASPL follows the shape of the directivity of BPF 1. It can therefore be concluded that, just as in the previous investigation, harmonic noise is the dominating noise source.

From the previously mentioned investigations about small UAV rotors, none considered the forward flight of a propeller configuration. For a propeller with close-to-axial inflow, the influence of a varying freestream velocity or propeller angle of attack are opposite when compared to the lateral inflow investigated by Yang et al. The axial flow velocity is given by $U_\infty \cos(\alpha_s)$ and the in-plane flow component by $U_\infty \sin(\alpha_s)$. This results in an increase in the cross-section angle of attack as the propeller angle of attack increases and a decrease in the in-plane flow component. Hence, for a constant RPM and freestream velocity, the thrust increases when the propeller angle of attack increases. The in-plane flow component determines then the strength of the asymmetry of the flow. A CFD analysis was performed to obtain the dynamic loading of the blade but no acoustic analysis was performed with this data. This leaves the question of how a numerical analysis of the noise spectrum of a small propeller at an angle of attack compares to experimental data, still one to be answered. Furthermore, the angular inflow that causes the unsteady loading contribution can be best investigated at BPF 1 [12].

2.5. Summary literature

To gain more insight in the unsteady motion of a propeller when it is placed at an angle of attack, different investigations conducted in the 80's and 90's were discussed. Larger scale propellers were positioned at a propeller angle of attack and showed a variation in loading of the blade over the azimuth. The noise levels increased for the first BPF and its harmonics, when compared to axial inflow. Two main causes for the increase in noise were found, as stated by Hanson: the unsteady loading and the increase in Mach number of the blade with respect to the observer. It was found that for a propeller operating at angular inflow, noise prediction theory is exact, in the sense that the noise prediction will be correct, when the blade loading and the blade geometry are correct.

Further inquiry led to several studies examining the forward flight of a multicopter propeller, experimentally and to some extent numerically. The forward flight of a multicopter propeller is mainly associated with lateral inflow. Similar to the large-scale propeller, the thrust varied significantly with the change of the az-

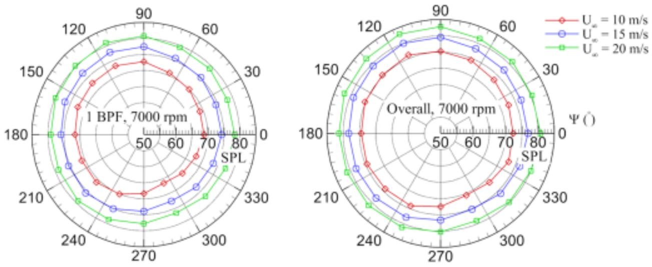

Figure 2.18: Comparison of SPL at different freestream velocities at RPM= 7000, $\alpha_s = 10°$ and $\Psi_{mic} = 0°$ [13].

imuthal position of the blade. Tonal noise occurred at BPF 1 and its harmonics. It was observed that for a constant RPM and propeller angle of attack, the tonal noise increased when the freestream velocity increased. Furthermore, for a constant RPM and freestream velocity, the thrust decreases due to an increase in propeller angle of attack, leading to a decrease in noise. It was observed that the OASPL followed the form of BPF 1 and hence the harmonic noise contribution is concluded to be the dominant noise source. To the author's knowledge, a full spectrum numerical noise analysis was not conducted for a small propeller at an angle of attack.

2.6. Research goals and questions

From the presented literature in this study, it can be observed that there is an absence in the analysis of small propellers at a small angle of attack. This propeller configuration is used in forward flight by, for instance, tilt-rotor UAVs and differs in that sense from a multicopter forward flight. The noise produced by this propeller configuration has been researched for larger rotors and only at the first harmonics but, to the author's knowledge, none has been conducted for small-scale propellers. Overall, a numerical analysis including both harmonic and broadband noise for a low Reynolds number propeller at a small angle of attack seems absent from literature. It can be argued that, for the sake of mission optimisation, this flight manoeuvre should be investigated.

The results of a quasi-steady modelling approach that corresponded well with the noise characteristics associated with a propeller at an angle of attack were discussed. This modelling method lies at the foundation of this thesis and is elaborated on in section 6.2. Building on the findings of the state of the art, some hypothesis about the noise spectrum of a small UAV can be formulated:

Hypothesis 1 (H1): *When the propeller is at an angle of attack with respect to the inflow, the harmonic component of the noise will increase for an observer under the flight path (as in Figure 2.9b), compared to operation in axial-inflow conditions.*

Hypothesis 2 (H2): *When the propeller is at an angle of attack with respect to the inflow, the harmonic component of the noise will decrease for an observer above the flight path, compared to operation in axial-inflow conditions.*

Where a propeller operating under steady conditions has varying aerodynamic properties along the span, an additional variation along the azimuth is introduced when the propeller is placed at an angle of attack. The azimuthal variation of the motion and its influence on noise while operating in the laminar-transitional Reynolds regime holds many uncertainties. In order to fill this gap the following research questions are posed:

1. What is the change in noise spectrum of a low Reynolds number, fixed pitch propeller when an unsteady motion is introduced by varying the angle of attack of the propeller from 0° to 7.5° and 15°?
    (a) What is the change in the harmonic noise contribution when a propeller angle of attack is introduced? *The variation in tip speed along the azimuth is expected to result in the onset of unsteady loading resulting in more pronounced tonal noise.*
    (b) How do the spectra measured directly above and underneath the flightpath compare? *When the rotor is tilted with respect to the freestream a difference in loading and radiation efficiency is expected above and underneath the flightpath.*
    (c) How do the different propeller angles of attack compare to each other? *The variation in tip speed along the azimuth changes with rotor angle of attack.*
2. How is the harmonic noise component affected by the unsteady motion introduced by a small angle of attack of the propeller when it is modelled by a quasi-steady modelling approach?
    (a) What is the change in blade loading along the azimuth when a propeller angle of attack is introduced? *The radiated noise due to unsteady loading is related to the variation in blade loading.*
    (b) What is the change in harmonic noise contribution when different angles of attack of the propeller are considered? *The change in noise contribution is an indicator of the variation in loading along the azimuth.*
    (c) How does the prediction of the harmonic spectrum compare to the experimental harmonic spectrum? *Relates to the applicability of the modelling approach.*

3

Experimental Setup

In this chapter, the experimental setup to investigate the effects of a propeller at an angle of attack on its noise spectrum is discussed.

3.1. Campaign Overview

The experiments for validation of the hypotheses is focused on capturing the noise emitted by a propeller at different angles of attack and the thrust and torque corresponding to each condition. Different conditions are measured to quantify the noise of the propeller. Two main setup configurations can be distinguished: one where the propeller is level and has no angle of attack with respect to the freestream. In the other condition the propeller is put at an angle with respect to the freestream. In these configurations different measurements are performed as indicated in Figure 3.1.

Three noise cases are measured in level configuration: Background noise measurements are performed to asses the noise levels of the room itself and to ensure that the measured signal is not contaminated by any noise of the surroundings. The background noise measurements are performed for different freestream velocities and angles. The rotor blades are not installed during these measurements.

Similar to the background noise measurements, the rotor blades are not mounted during the motor noise measurements. The motor noise is measured at zero freestream velocity and different RPM's. The motor noise is similar for the cases at at an angle of attack.

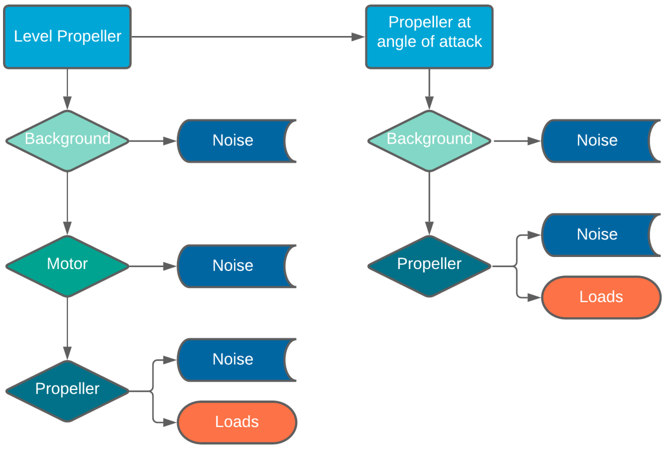

Figure 3.1: Overview of the different elements of the wind tunnel experimental campaign.

3.2. A-tunnel

The experiments are performed in the A-tunnel of Delft University of Technology. The A-tunnel is vertical wind tunnel through which the flow moves from below through an open test section. The exit of the the wind tunnel is circular and has a diameter of 0.6m. The contraction ratio of the exit nozzle 15:1. The turbulence level of the tunnel is very low, smaller than 0.1 at flow velocities of 10 m/s and higher [48]. The A-tunnel allows for aeroacoustic measurements up to 35 m/s with this nozzle. The ceiling and walls surrounding the test-section are treated with melamine acoustic wedges. For a detailed description of the wind tunnel and its acoustic features the reader is referred to the paper of M. Merino et al. [49].

3.3. Experimental setup

In this section a description of the experimental set-up is presented. First the propeller is described, after which the test set-up and the different set-up configurations are discussed.

The propeller used in this experiment has a tip radius, R_{tip} of 15 cm and a single profile along the span: the NACA4412. At the root, an elliptical section morphs into the profiled section. The hub-radius is 1.25 cm long. In Figure 3.2a a CAD drawing of the blade can be found. The blade chord and twist of the profile sections along the span are presented in Figure 3.2b. The maximum pitch angle of the blade is 43.6° and the maximum chord length is 3.4 cm. The propeller is powered by a 3536 1520KV brushless outrunner motor from Leopard Hobby. The motor has a maximum loading of 48 A, a maximum power of 550 W, 14 magnetic poles and measures 27.8 mm in diameter. The power to the motor is supplied by a Delta Elektronika DC power supply with an operational current range of 0 to 100 A and a voltage range of 0 to 15 V. The assembly of the motor spacer and loadcell, to which the propeller is attached, is placed in an aluminium nacelle with a diameter of 7.5 cm. The nacelle is put around the assembly to minimise its interference with the flow.

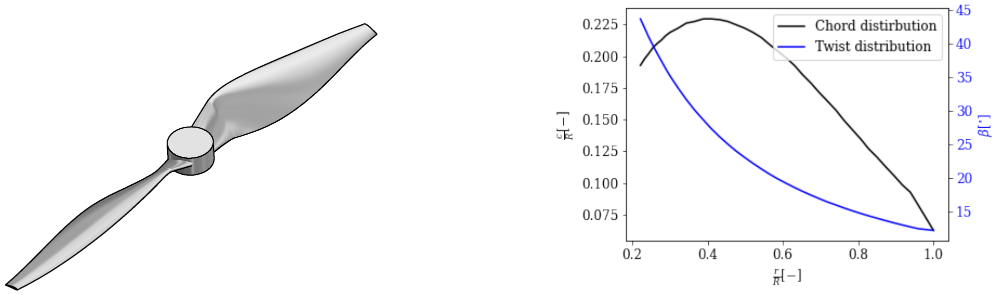

(a) CAD render of propeller geometry.

(b) Propeller chord and twist distribution.

Figure 3.2

The experimental set-up is mounted on top of the nozzle of the wind tunnel. Four steel bars with a diameter of 4 cm are installed to hold the nacelle in place. A NACA0012 profile of 8 cm chord length and 1.20 m width is attached to a nacelle in which the motor, cooling devices are positioned. The wiring of the of all the components inside the nacelle is lead through the NACA profile outside of the jet of the win tunnel. Two clamps in the form of the wing profile hold the nacelle structure and ensure a solid connection with the steel rods. The rods that hold the structure are placed 5 cm off centre to ensure that the propeller centre is aligned with the centre of the wind tunnel nozzle. The set-up is shown in Figure 3.3a. The propeller centre is positioned 4 propeller diameters from microphone 14 installed on the array, as indicated in Figure 3.3b[1]

To mimic a simultaneous measurement of the noise in an *above* and *below* the flight path configuration, the nozzle on the exit of the wind tunnel with the set-up on top of it is turned 180°. In Figure 3.5a, the configuration of the set-up with respect to the microphone array is shown that corresponds to *below* the flight path. In accordance with Hanson, the location of microphone 14 is set to 270° with respect to the propeller centre [50]. This configuration is from now on referred to as array configuration 1. In a similar way, in Figure 3.5b, configuration 2 of the set-up is presented in which the microphone array is located *above* the

---

[1] The numbers in the sketch are merely to indicate the *amount* of microphones mounted vertically. The only number corresponding to its microphone number is the centre microphone, number 14. This is also the case in Figure 3.5a and Figure 3.5b.

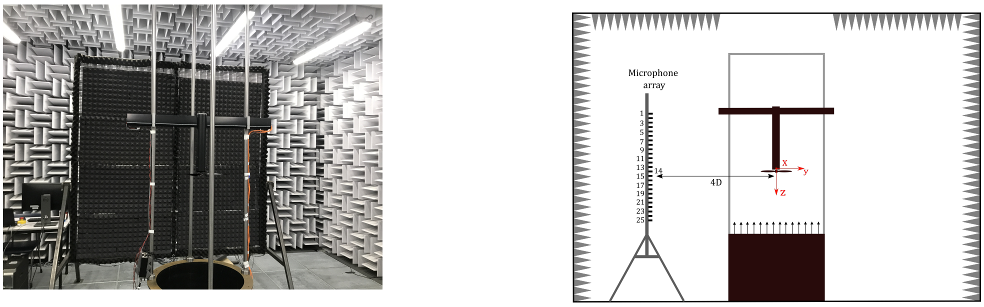

(a) Propeller set-up mounted in front of the microphone array in the A-tunnel at TU-delft.

(b) Schematic drawing of the propeller set-up mounted in the A-tunnel.

Figure 3.3

flight path of the propeller. In array configuration 2, the position of microphone 14 corresponds to an angle of 90° with respect to propeller centre.

3.4. Measurement Techniques

Different measurement techniques and devices were employed to enable measurement of the propeller performance and its noise emission. This section elaborates on the techniques that were used. In subsection 3.4.1, a description is given of the the propeller noise measurements set-up and in subsection 3.4.2, the propeller performance methods are elaborated.

3.4.1. Propeller noise measurements

The propeller noise measurements are performed with 50 G.R.A.S 40 PH free field microphones with integrated CCP preamplifiers [51]. The microphones are mounted on an array, which measures 2 m by 2 m. Their positions are specified in Figure 3.4. The distance between the microphones is 7.5 cm from centre to centre. The centre microphone of the array is positioned at a lateral distance of 1.2 m with respect to the propeller centre outside the jet of the stream.

The microphones have a diameter of 7 mm and operate in the frequency range of 10 to 20 Khz with a frequency response of ±1 dB. The maximum sound pressure level is 135dB. The microphones are calibrated with a G.R.A.S. Pistonphone. A sampling frequency of 51.2kHz is used for each noise measurement. The acquisition system for the microphone system consists of a National Instrument PXIe-4499 sound and vibrations data acquisition module. The duration of the measurements varies with the type (background, motor, or propeller) of noise that is measured and is indicated in Table 3.1.

3.4.2. Propeller performance measurements

The Wyler clinotronic plus inclination sensor was used to determine the angle of attack of the nacelle and hence the propeller. The sensor is able to measure the absolute angle of the surface it is placed on over a range of ±45° and has a resolution of 0.01° [14].

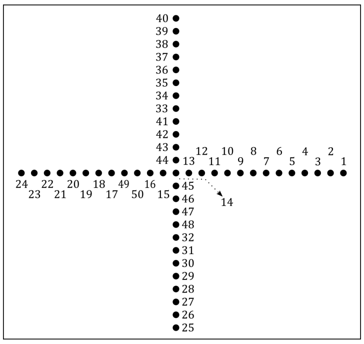

Figure 3.4: Microphone positions of the microphone array, the visual position of the array corresponds to the position left of the microphone array, as depicted in Figure 3.3b.

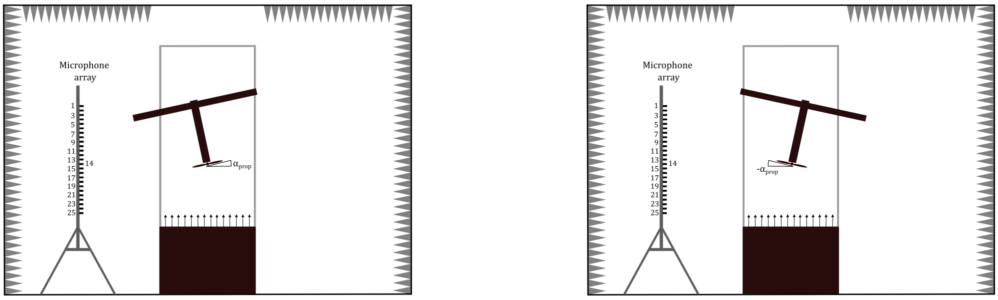
Microphone array
1
3
5
7
9
11
13
15
17
19
21
23
25
14
α_{prop}
Microphone array
$-\alpha_{prop}$

(a) Set-up configuration array 1.

(b) Set-up configuration array 2.

Figure 3.5: Schematic representation of microphone array configuration 1 and 2.

Type of measurement	Duration [s]
Background	20
Motor	20
Propeller	30

Table 3.1: Acquisition time for different noise measurements.

To measure the forces and moments, the ATI Mini40 F/T transducer with axial cable was integrated into the setup. It has a thickness of 12.27 mm and a diameter of 40.1 mm. For the three Cartesian coordinates the transducer is able to measure the forces and moments. The transducer system exists of the transducer itself, a data acquisition system and a shielded cable [15]. The signal is provided by silicon strain gauges in volts and then amplified and converted to digital data by the data acquisition system. The measurement range of the loadcell is presented in Table 3.2 together with the measurement uncertainty. The measurement uncertainty is given in percentage of the full load and express the maximum amount of error for each axis [17]. Furthermore, the operational temperature of the loadcell ranges from 0 to $100°C$. A deviation of ±5°C from 22° leads to a typical gain error of 0.1%. The error increases to 0.5% when the temperature deviation is increased to ±5°. The sampling frequency used is 1000Hz and the measurement time was 10 seconds. A schematic drawing of the loadcell can be found in Figure 3.6b. A thermocouple was used to measure the temperature of the loadcell.

3.4.3. Oil-flow visualization

The flow over the blade is visualized by means of an oil-flow visualization. A layer of mixture of liquid paraffin wax and fluorescent oil is applied to the suction side of the blade. The blade is then run for about 8 minutes at constant conditions. Because of the density of the oil, the oil remains attached to the blade in the zones where the flow is separated and follows the shape of the streamlines there.

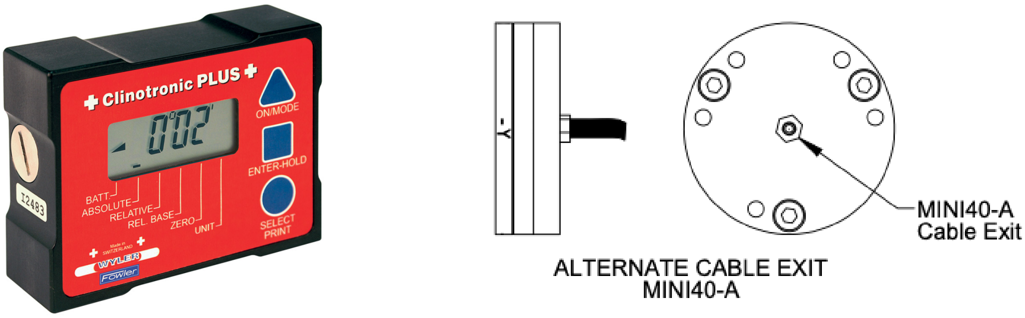
Clinotronic PLUS
0.02
ON/MODE
ENTER-HOLD
SELECT PRINT
BATT
ABSOLUTE
RELATIVE
REL. BASE
ZERO
UNIT
WYLER
Fowler
12483
MINI40-A Cable Exit
ALTERNATE CABLE EXIT
MINI40-A

(a) Wyler clinotronic plus inclination sensor [14].

(b) Schematic drawing of the loadcell with alternate cable exit [15].

Figure 3.6

	Fx	Fy	Fz	Tx	Ty	Tz
Calibrated range(±)	20 N	20 N	60N	1Nm	1Nm	1Nm
Measurement uncertainty (percent of full load)	1.25%	1.00%	0.75%	1.25%	1.25%	2.00%

Table 3.2: Operational range of loadcell and measurement uncertainty [17].

3.5. Measurement Post-Processing

The ATI loadcell outputs six channels corresponding to the force and moment components. The zero loading off sett is determined by means of a bias measurement. This is used to obtain the actual forces and moments produced by the propeller. This is elaborated on in subsection A.1.1. A detailed description of the error quantification of the loadcell can be found in [52].

For noise post processing, the data signal of the microphones was converted to the frequency domain using Welch's method [53]. An overlap of 50% was used together with a Hamming window. The window length was chosen such that the frequency resolution ranges between 1 and 4 Hz. Furthermore, because of the small free stream Mach numbers used in the experiments, it is assumed that shear layer refraction will not have a significant effect on the recorded directivity patterns [13].

4

Propeller performance

The performance of the propeller was measured to quantify the thrust and torque of the propeller. In this chapter, a brief overview of the propeller performance at zero angle of attack is given. First an overview of the measurements is presented, after which the loads of the propeller at an angle of attack are presented.

4.1. Zero angle of attack

The propeller performance measurements at zero propeller angle of attack were performed to obtain a data set to validate the steady simulation. In order to be able to validate the steady model by Xrotor, a series of measurements were performed corresponding at 4000 RPM and values of J. J is changed by altering the freestream velocity.

Case	V_∞[m/s]	J[-]	$Re_{0.75} \cdot 10^4$
1	0	0	7.38
2	2.4	0.12	7.40
3	4.8	0.24	7.42
4	7.2	0.36	7.47
5	8.0	0.4	7.49
6	9.6	0.48	7.53
7	12.0	0.6	7.62
8	14.4	0.72	7.72
9	16	0.8	7.80

Table 4.1: Propeller performance measurement case matrix for zero propeller angle of attack and RPM = 4000.

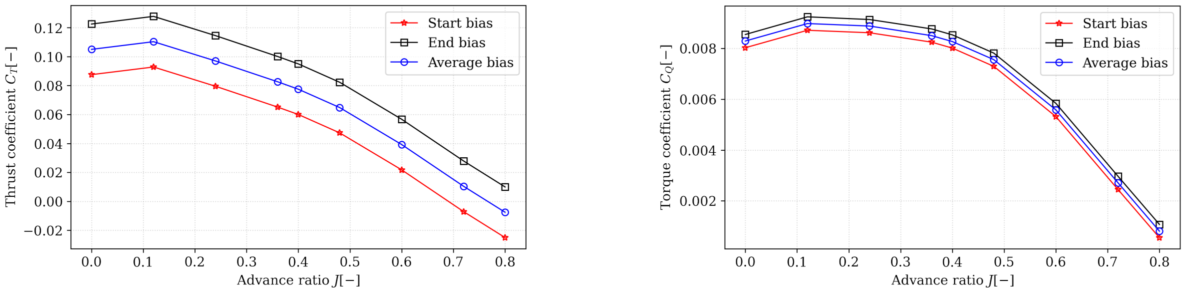

(a) Thrust coefficient corrected with bias measurements.

(b) Torque coefficient corrected with bias measurements.

Figure 4.1: Bias measurements comparison at at RPM = 4000 for a range of J.

In Figure 4.1, the thrust and torque coefficient corrected with the different bias values are presented. Since the set-up was not physically altered during the measurements, the difference in bias is noted as uncertainty.

The thrust and torque coefficients corrected with the bias measurements are presented in Figure 4.2, together with the propulsive efficiency. A parabolic trend with its maximum value at $J = 0.12$ is observed for the thrust coefficient. This trend is also in line with observations by other authors for small propellers [3], [54]. From $J = 0$ to $J = 0.4$ the root sections of the blade are separated, increasing the drag of the blade and contributing to the high torque values found in this range. For higher advance ratios the torque decreases due to a reduction in drag. The reduction in drag is caused by the reduction of the section angle of attack below stall angles [55]. The trend of the propulsive efficiency is expected to be the opposite of the torque: with a decrease in torque, the efficiency increases to a maximum value of 0.67 at $J = 0.6$.

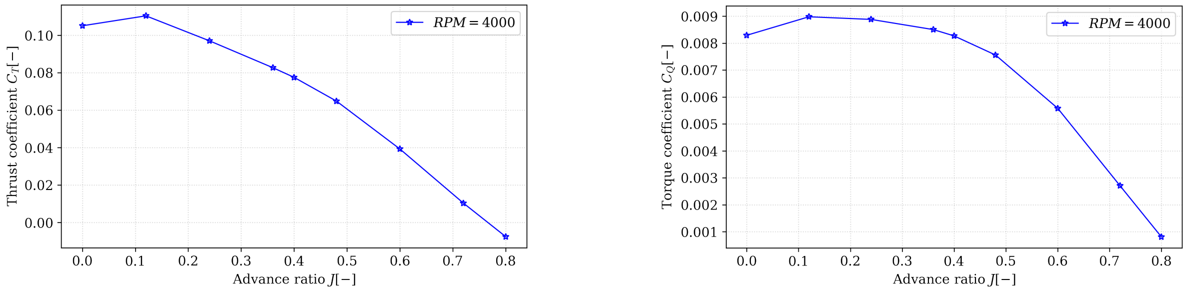

(a) Thrust coefficient. (b) Torque coefficient.

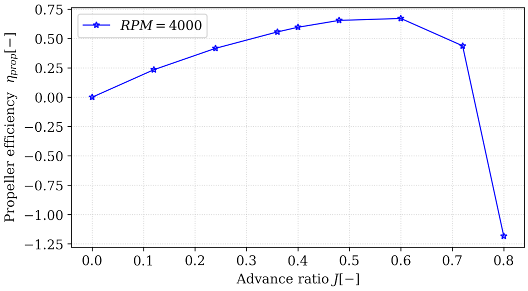

(c) Propulsive efficiency.

Figure 4.2: Propeller performance over a range of J at RPM = 4000.

5

Propeller Noise

In this chapter, an overview of the noise measurements is presented. First, the different noise sources are identified in section 5.1. Next, in section 5.2, an analysis of the effect of the propeller angle of attack on noise is given with respect to the hypothesis (which were presented in section 2.6).

Before the experimental results are presented a few caveats have to be discussed with regard to the experiment. First of all, the variability of the RPM is not captured during the experiments. Because the RPM variability adds to the variation in speed around the azimuth, this might cause unexpected variations in the noise spectrum due to an increase or decrease in unsteady loading. Furthermore, it is not known if the RPM variability is affected by the propeller angle of attack. Moreover, no quantification of the noise level variation between measurements has been obtained. It is therefore unknown what the variation in trends and magnitudes will be when the experiment is repeated.

5.1. Identification of different noise sources

In this section an overview is given of the identified noise sources in the spectra. First a comparison between the propeller noise and the motor and background noise of the wind tunnel is given for an advance ratio of 0. Next, the advance ratio is increased and the changes are described.

In Figure 5.1a, the background noise of the wind tunnel, the noise produced by the motor (without freestream velocity) and the noise produced by the propeller are plotted at an advance ratio of $J = 0$, together with the background noise of the tunnel. The background noise is measured to establish the noise present in the room and to identify any noise sources that are present. In an ideal case, the background noise goes down with a straight line and a difference between the noise source of interest and the background noise level is around 10 dB [56]. For $J = 0$ this is the case for most of the spectrum.

The motor noise shows a peak at BPF 0.5 (67 Hz). Furthermore, a large bump ranging from 500 Hz to 19 kHz can be observed which is mainly due to the motor and vibrations of the structure. In this range some distinct tones are also present. When the motor is loaded, the noise emitted by the motor is likely to change [55]. Motor noise emitted by the installed propeller configuration might therefore differ considerably from the noise produced by the isolated motor. Due to loading of the motor, e.g. by the propeller, discrete tones

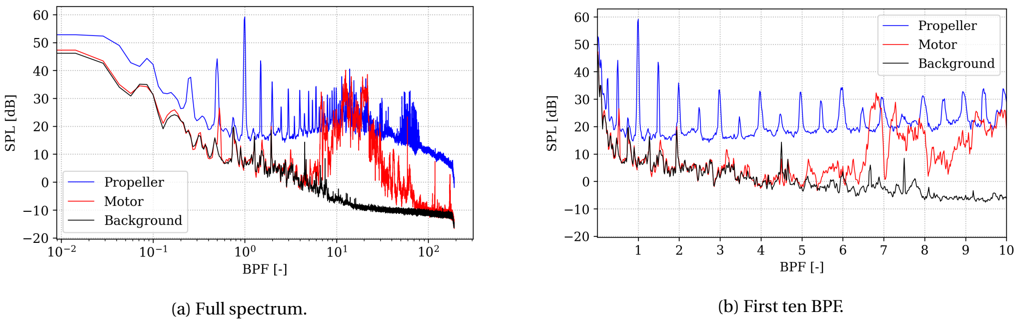

(a) Full spectrum.

(b) First ten BPF.

Figure 5.1: Background, motor and propeller noise measured with mic_{14} at RPM = 4000, $J = 0$ with a level propeller configuration.

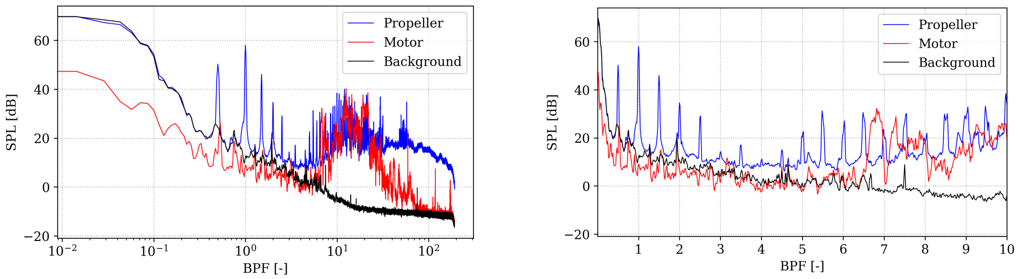

(a) Full spectrum.

(b) First ten BPF.

Figure 5.2: Background, motor and propeller noise measured with mic_{14} at RPM = 4000, $J = 0.4$ with a level propeller configuration.

appear at the multiples of the motor shaft rotational frequency (BPF $n+0.5$). These are assumed to be due to unbalanced loading of the motor shaft [57], [58]. This can be seen clearly when the peaks at 67 Hz and 200 Hz are examined. After the main harmonic at BPF 1, the harmonics BPF 0.5 and BPF 1.5 exhibit the greatest magnitude in the spectrum. Furthermore, the motor noise influences the spectrum from BPF 7 onwards, Figure 5.1b, and hence for the harmonic analysis in this thesis only the first 6 BPF are considered.

At BPF 1 and its multiples ($n\cdot$ 133.33 Hz) distinct tones are present. This becomes more clear when Figure 5.1b is examined. The most pronounced tone is at BPF 1 and is mainly due to the steady loading of the blade [59]. As can be observed, the sound radiated by the propeller persists beyond the BPF at higher frequencies. A decreasing trend in SPL can be observed for BPF 2 and 3. BPF 4 up until BPF 6 are of the same order of magnitude. The persistence of the higher order multiples of the BPF are said to be due to non-uniformity of the flow [60]. Beyond BPF 6, the propeller signal is contaminated with motor noise.

When a freestream velocity is introduced, increasing the value J, the spectrum changes when compared to the $J = 0$ case. In Figure 5.2a, the spectrum obtained at $J = 0.4$ is presented. The propeller noise for low frequencies follows the shape of the background noise. The motor noise measured at BPF 0.5 and BPF 1.5 appears to increases with respect to the $J = 0$ case. The high frequency bump due to the motor is of similar magnitude. In the range of 300 Hz to 800 Hz, a decrease in SPL can be observed with respect to the $J = 0$ case. The distinct peaks that could be identified in Figure 5.1a in this frequency range are now less pronounced or even not present. In the $J = 0$, these tones are associated with unsteady blade vortex interaction noise because the wake is not convected by the freestream [61]. When the high frequency range of the propellers are compared, a bump can be identified. This bump was less pronounced when no freestream velocity was present. In the $J = 0$ case, almost no bump is present from 4000 Hz to 20.000 Hz. Furthermore, the spikes concentrated around 10.000 Hz are less pronounced and have less width than in the $J = 0$ case.

In Figure 5.2b, a clear decrease of BPF 1 can be observed when compared to the hover case at $J = 0$, this is due to the reduction in thrust. Furthermore, a reduction of BPF 2 to BPF 4 is observed. Due to the freestream, the wake of the rotor is convected and hence unsteady pressure fluctuations originating from the interaction between blade and vortex are reduced. At BPF 3 and BPF 4, almost no tone is present anymore. Hereafter, the SPL of the BPF multiples increases again.

The spectrum obtained at an advance ratio of $J = 0.6$ is presented in Figure 5.3a. For the background noise, similar trends case can be observed as for the $J = 0.4$ case, although they are found to be 5 to 10 dB

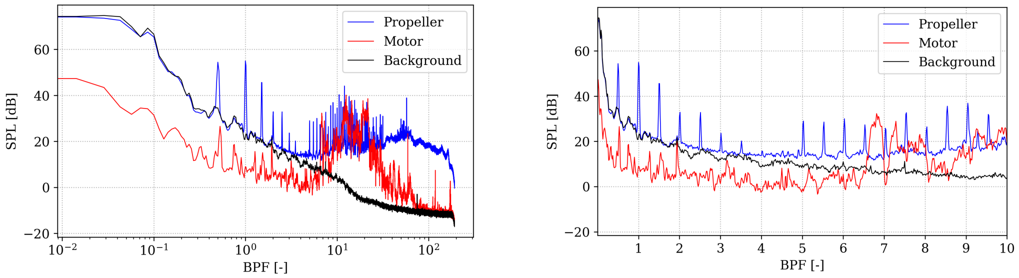

(a) Full spectrum.

(b) First ten BPF.

Figure 5.3: Background, motor and propeller noise measured with mic_{14} at RPM = 4000, $J = 0.6$ with a level propeller configuration.

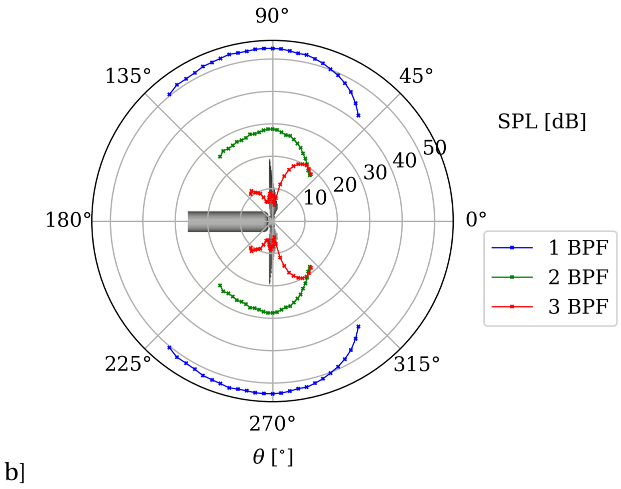

Figure 5.4: Directivity of first three BPF at RPM= 4000, $J = 0.4$ and $\alpha_r = 0°$.

higher over the full spectrum due to the higher freestream velocity. The motor noise, measured at BPF 0.5 and BPF 1.5, appears to increase with respect to the $J = 0.4$ case, giving rise to a tone at BPF 0.5, which is almost equal in magnitude to BPF 1. A further increase in the SPL of the high frequency broadband bump, ranging from 4000 Hz to 20.000 Hz can be observed. When Figure 5.3b is examined and compared to Figure 5.2b, the magnitude of BPF 1 and 2 are lower than in the $J = 0.4$ case. This is because of the reduction in loading on the blade at higher advance ratios.

Overall two effects can be identified, first, the background noise increases when the advance ratio is increased. Secondly, with an increase of the advance ratio, the blade loading goes from heavily loaded to lightly loaded, and correspondingly the BPF 1 harmonic decreases in magnitude.

5.1.1. Directivity

In Figure 5.4, the directivity of the first 3 BPF are plotted, scaled to an observer distance of 1.5 m. The first and second BPF show a clear directivity pattern with a maximum value reached at about $\theta = 90°$. The third BPF radiates towards the 55° and 305° at SPL levels of 10 dB.

5.2. Noise emissions from a propeller at an angle of attack

In this section the experimental results relating to the propeller angle of attack are discussed briefly. First, the noise at two different angles of attack is assessed at two different microphone positions: *underneath* and *above* the flightpath, corresponding with array configuration 1 and 2, respectively. For readability purposes, the setup of the different configurations is presented again in Figure 5.5.

In Figure 5.6a, the full spectra of the propeller at an angle of attack of $\alpha_r = 7.5°$ are presented and compared to the spectra of the level propeller at $\alpha_r = 0°$, in Figure 5.6b the first 6 BPF are shown. The operating conditions are $J = 0.4$ at an RPM of 4000 which corresponds to a freestream velocity of 8 m/s.

Two main features can be observed when the plots in Figure 5.6 are inspected. For the first 3 BPF an

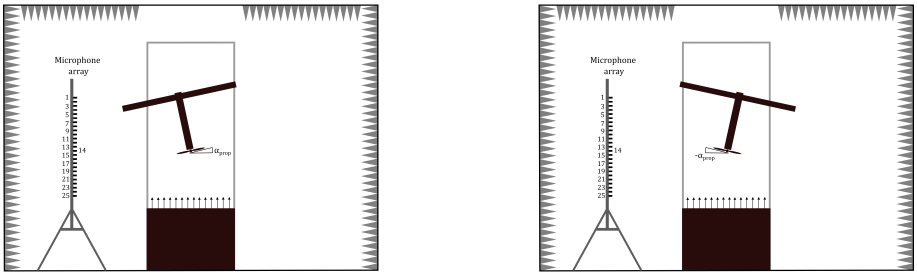

(a) Setup configuration array 1.

(b) Set up configuration array 2.

Figure 5.5: Schematic representation of microphone array configuration 1 and 2.

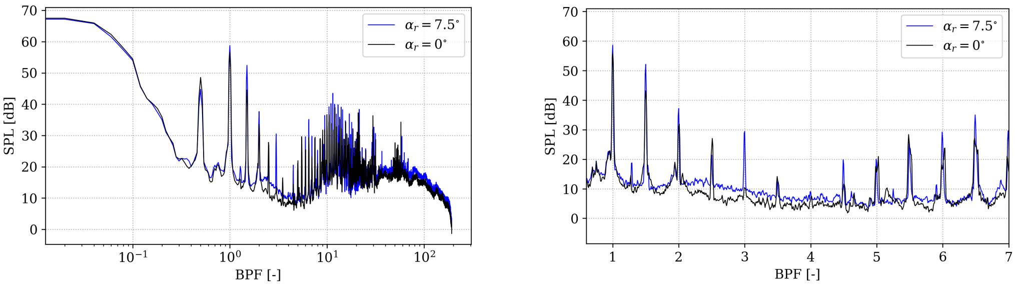

(a) Full spectrum.

(b) First 6 BPF.

Figure 5.6: Propeller noise measurement with array configuration 1 at RPM = 4000, $J = 0.4$ with mic_{14} and $\alpha_r = 7.5^\circ$.

increase in SPL can be observed with respect to the level propeller, in line with H1. As this array configuration corresponds to the flightpath underneath the propeller, an increase in these peaks is expected due to the unsteady loading of the blade as well as the velocity effect with respect to the observer. BPF 4 and BPF 5 show little difference between the level and rotor angle of attack case. BPF 6 follows the trend of the first 3 BPF. Secondly, the broadband hump, identified from 4000 Hz to 20.000 Hz in Figure 5.6a, shows a larger SPL at an angle of 7.5° when compared to the level propeller.

When the propeller angle of attack is increased to $\alpha_r = 15^\circ$, presented in Figure 5.7, similar observations can be made with respect to the level propeller. In Figure 5.7b an increase of the first 3 BPF can be examined. Furthermore, when the different angles are compared, an increase of the first 3 BPF can be observed with an increase in rotor angle of attack. Little to no difference is found for the BPF 4 and BPF 5, while BPF 6 follows the trend of the first 3 BPF again. Furthermore, the broadband hump increases with increasing rotor angle of attack.

In Figure 5.8, measurements are performed with array configuration 2 at a rotor angle of attack of $\alpha_r = 15^\circ$. For array configuration 2, the SPL is expected to decrease with respect to the level propeller. It is observed from Figure 5.8a that the main harmonic noise component is due to the first BPF. A different trend can be observed when it is compared to the SPL of the level propeller, as it decreases with increasing angle of attack. With an increase in angle of attack, the noise measured at BPF 1 decreases, this is in line with H2. A similar trend is observed for the second BPF where the noise emissions of the propeller at an angle of attack are lower than that of the propeller at zero angle of attack. BPF 3 does not follow the trend of BPF 1 and 2. BPF 4 and 5 show similar characteristics as with array configuration 1 and BPF 6 seems to follow the trend of BPF 1 and 2.

When the angle of attack of the propeller is increased to $\alpha_r = 15^\circ$, a further decrease of BPF 1 and 2 can be observed, Figure 5.9. The higher harmonics, in Figure 5.9b, follow similar trends to the $\alpha_r = 7.5^\circ$ case.

5.2.1. Directivity

In order to illustrate the effect of the angle of attack of the rotor on the directivity pattern, the directivity of the first BPF and the OASPL of the first 6 BPF are presented in Figure 5.10. The image of the propeller is for illustration purposes only and is presented to indicate the position of propeller with respect to the microphones. It is stressed that changing the angle of the propeller also changes the respective angle of the

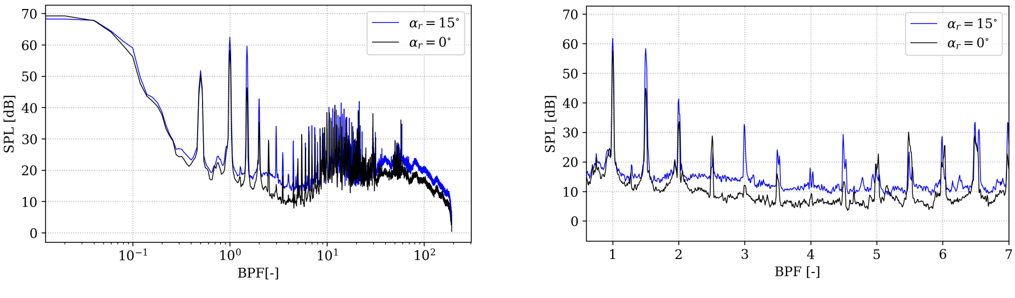

(a) Full spectrum.

(b) First 6 BPF.

Figure 5.7: Propeller noise measurement with array configuration 1 at RPM = 4000, $J = 0.4$ with mic_{14} and $\alpha_r = 15^\circ$.

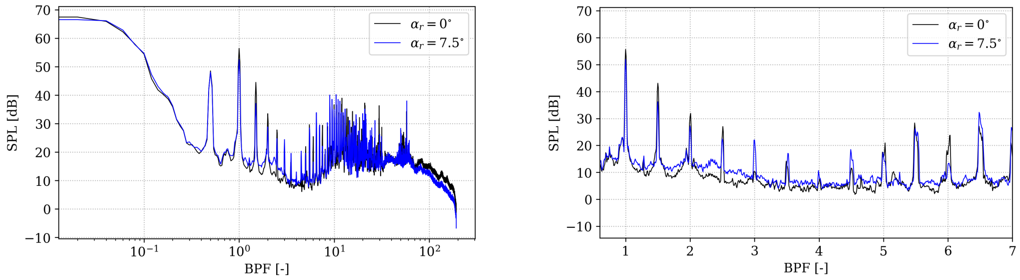

(a) Full spectrum.

(b) First 6 BPF.

Figure 5.8: Propeller noise measurement with array configuration 2 at RPM = 4000, $J = 0.4$ with mic_{14} and $\alpha_r = 7.5°$.

propeller axis and the microphones. When $\alpha_r = 0°$, the propeller axis is aligned with the horizontal 0° line.

From Figure 5.10a, it becomes clear that there is a difference between SPL measured above and underneath the propeller. For the observers placed underneath the flightpath, it is clear that when the rotor angle of attack increases, the SPL increases for BPF 1. An opposite trend is expected above the rotor and at $\theta = 90°$, it can be observed that the SPL decreases with increasing angle of attack. However, it seems that the directivity of the $\alpha_r \neq 0°$ cases does not follow the expected trend: a minimum is expected at the rotor axis while in Figure 5.10a, both the rotor angle of attack cases show a decrease from 70° to a minimum at about 55°. After which an increase for both cases can be observed of what appears to be a second lobe. The minimum appears at the same location for both the cases. The directivity pattern appears only for array configuration 2 and for a non-zero rotor angle of attack. A possible explanation for this could be that the local minimum and the appearance of a secondary lobe are the result of reflective interference from the structure or the microphone array. The acoustic treatment of the room avoids reflection above 150 Hz, while BPF 1 is at 133.33 Hz [49]. Furthermore, similar observations were made by other authors [9], [62]. Axial directivity patterns were found for BPF 1 that consisted of multiple lobes, thought to be caused by reflections or other interference, this is shown in Figure 5.11. At a visual angle of 60° the measurements obtained at a pitch angle from −10° to +5° show minimum. At a visual angle of 120°, another minimum can be witnessed for all pitch angles. According to the authors the side lobes are not indicative of the axial directivity of propeller noise.

In Figure 5.10b the OASPL of the first 6 BPF (110 to 805 Hz) is presented for the different array configurations. A range of 5 Hz is left out at BPF 1.5 (200 Hz) because of excessive motor noise. A similar trend as with BPF 1 can be observed for the observer position underneath the flightpath. Above the flightpath a decrease of the OASPL is observed between the non-zero angle of attack cases and the level propeller for an observer placed between 50° and 130°. From 50° and 75°, when the observer position is placed towards the observer axis, a decrease in OASPL can be examined for the $\alpha_r = 15°$ case.

5.2.2. Discussion

From the presented experimental results, it can be concluded that there is a difference between the noise radiation above and underneath the propeller. The trend underneath the rotor is clearly visible: with an increasing angle of attack the noise levels increase: bearing in mind the limited quantification of measurement errors, H1 is confirmed.

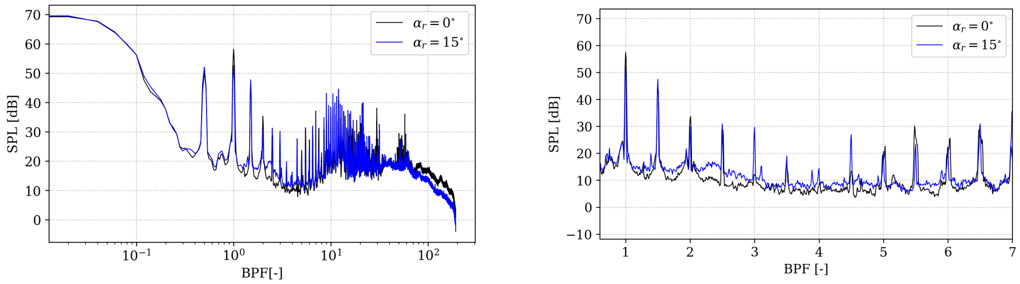

(a) Full spectrum.

(b) First 6 BPF.

Figure 5.9: Propeller noise measurement with array configuration 2 at RPM = 4000, $J = 0.4$ with mic_{14} and $\alpha_r = 15°$.

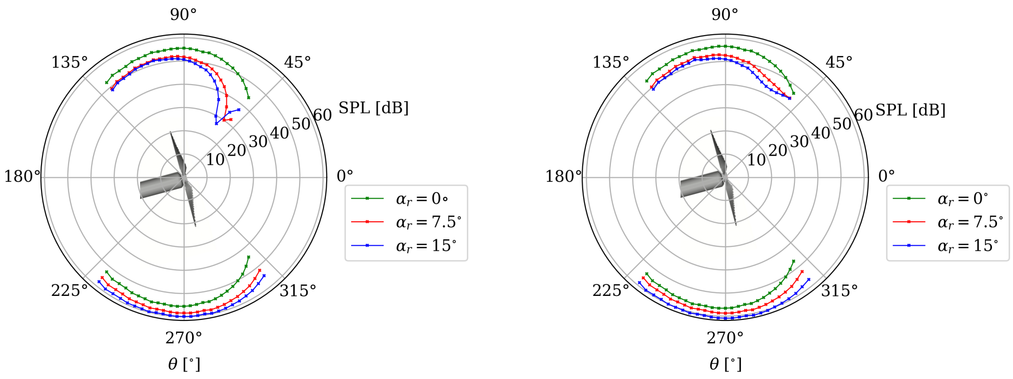

(a) Directivity of the BPF 1.

(b) OASPL from BPF 1 to BPF 6 (110 to 820 Hz) with BPF 1.5 removed.

Figure 5.10: Directivity of the SPL with array configuration 1 ($\theta = 0^\circ$ to 180°) and 2 ($\theta = 180^\circ$ to 270°) at RPM = 4000, $J = 0.4$ for different α_r.

For H2, to draw a similar conclusion a little more background is necessary: unsteady loading increases the noise levels while a reduction in the velocity of the blade, encountered above the propeller in the direction of the microphones, decreases the noise level [63]. Another reason for the small difference between the $\alpha_r \neq 0$ cases above the propeller, beside the uncertainties mentioned at the beginning of this section and the discussion of anomalous experimental results at BPF 1, could be that the decrease of the velocity of the blade in the direction of the observer is counteracted by the increase in noise levels of the unsteady loading. Furthermore, with a decrease of the harmonic noise sources, the relative contribution of other noise sources, e.g. motor noise, become more prominent. However, the OASPL above the propeller shows a decrease in noise with respect to the $\alpha_r = 0$ case when the noise at BPF 1.5 is omitted. It is concluded, in accordance with literature, that H2 is also confirmed [9].

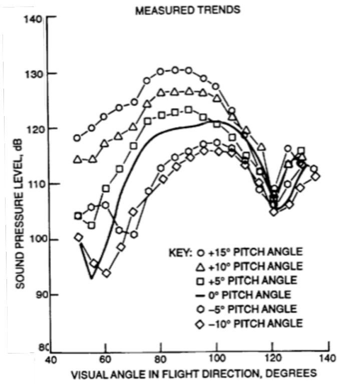

Figure 5.11: BPF 1 at different rotor pitch angles [9].

6

Analytical Methodology

For this thesis, different methods of computation are employed. All of them are implemented in Python. A general overview of the programme flow is presented in Figure 6.1. The analysis firstly requires the definition of the blade geometry, the operating conditions and the different computational settings. After definition of the input variables, the propeller performance is simulated. A steady simulation programme will be expanded to a quasi-steady model, which should be able to approximate the performance of a propeller at an angle of attack. To asses the noise of the propeller, the propeller performance data is used as input for the noise module. The results can be processed and analysed at this point, after which the tool is stopped. In section 6.1, the steady simulation tool is elaborated on and its workflow is explained. This section also contains information about the input variables of the simulation programme and how they are obtained. In section 6.2, the steady simulation is expanded to a quasi-steady simulation. Finally, in section 6.3, the method for calculation of the propeller noise is discussed.

6.1. Propeller performance prediction

At the basis of the quasi-steady modelling scheme used for this thesis, lies a steady simulation programme. This section follows the structure of the flowchart for the steady load calculation presented in Figure 6.2. The propeller modelling tool implemented in this thesis is Xrotor [1]. Xrotor is a propeller modelling tool used at the Flight Performance and Propulsion department of TU Delft. Xrotor can be used to asses the performance of propeller and even propeller design. The flowchart of the steady propeller performance modelling is presented in Figure 6.2. In subsection 6.1.1, details about Xrotor are presented.

6.1.1. Xrotor

Xrotor is a propeller performance and design analysis programme based on classical propeller lifting line theory. Through iteration, Xrotor is able to calculate the circulation and the induced velocities, the local angles of attack and the lift and drag coefficients. Xrotor outputs a data file containing all this information when convergence of the iteration is achieved.

Xrotor provides three methods for calculation of the induced velocities and induced losses. In Xrotor, the

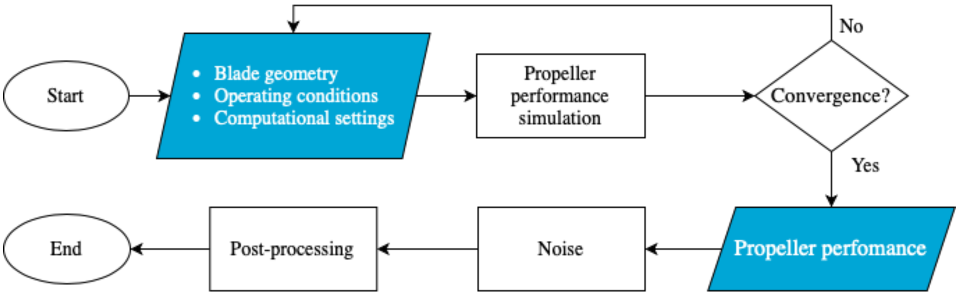

Figure 6.1: Blade section angle definition and components of the velocity triangle, adapted from [2].

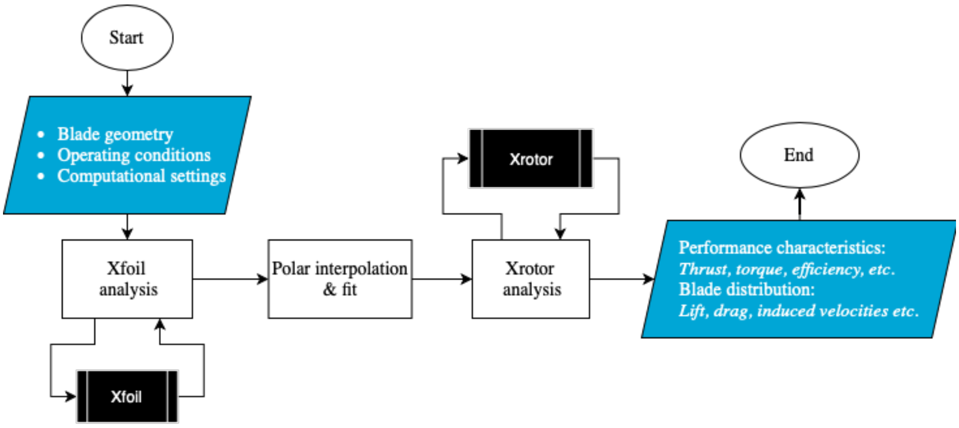

Figure 6.2: Flowchart for calculation of the steady loading of the propeller.

standard computation method for the axial and tangential induced velocities, u_a and u_t, respectively, is performed using the potential formulation. In the potential formulation, the induced velocities are determined through an exact potential flow field about the helical vortex field. The potential formulation used in Xrotor is an extension of the Goldstein's solution for two and four bladed propellers [64].

In order for Xrotor to run, the program requires several different input parameters: a list of aerodynamic section variables, which can be found in Table 6.1 and are elaborated on in subsection 6.1.2, and a geometry of the blade. The geometry is dependent on several variables of which three are given over the span of the wing for each radial station.

The input variables are the non-dimensional radial location of each blade station, represented by $\frac{r}{R}$, the non-dimensional local chord, given by $\frac{c_{loc}}{R}$ and the local twist angle, $\beta(r)$. Furthermore the amount of blades, B, is required together with the tip radius, R_{tip}, the radius of the hub, R_{hub} and the freestream velocity for which you design the geometry. For each individual blade section, the Reynolds number is determined, after which the polars are generated with XFoil. A fitting is applied to the polars, through which the parameters in Table 6.1 are determined.

Xrotor includes a correction for Reynolds number effect and an increase in drag at Mach numbers above the limit of the critical Mach number. In Equation 6.1, the drag determined by Xrotor can be identified. It is dependent on various variables given in Table 6.1. Note that the drag coefficient is scaled by the Reynolds number seen by the blade section, indicated by Re, the reference Reynolds number and an exponent f. The value of the Reynolds scaling exponent should be selected from the following list [1].

Note that the relation for the drag is reduced to a quadratic relation and that it might not be able to fully capture non-quadratic $C_d - C_l$ behaviour that might occur due to low Reynolds numbers or airfoil shape.

$$C_{d,Xrotor} = \left[C_{d_o} + \frac{dC_d}{dC_l^2}(C_{l_0} - C_l)^2\right]\left(\frac{Re}{Re_{ref}}\right)^f + k(M - M_{crit})^n \tag{6.1}$$

- $-0.2 < f < -0.1$ for high-Reynolds turbulent flow, $Re > 2 \cdot 10^6$
- $-0.5 < f < -1.5$ for low-Reynolds, $2 \cdot 10^5 < Re < 8 \cdot 10^5$
- $-0.3 < f < -0.5$ for mostly-laminar airfoils, $Re < 1 \cdot 10^5$

6.1.2. Aerodynamic section properties

To determine the lift and drag coefficients of each blade section, Xrotor requires airfoil section properties to be defined. The airfoil section properties exist of a number of airfoil parameters, which are used by Xrotor to reconstruct the airfoil specific polars from which they are derived. Xfoil generates polars, after which a fitting is applied and the input variables required by Xrotor are derived. A guide to fit the polars is provided by Drela [65]. The different variables are presented in Table 6.1.

Quantity	Description
α_0	Angle of attack at which $C_l = 0$
$\frac{dC_l}{d\alpha}$	Lift curve slope
$\frac{dC_l}{d\alpha}_{stall}$	Lift curve slope after stall
$C_{l_{max}}$	Maximum lift coefficient
$C_{l_{min}}$	Minimum lift coefficient
ΔC_l	C_l increment to stall
C_{d_0}	Minimum drag coefficient
C_{l_0}	Lift coefficient at minimum drag value
$\frac{dC_d}{dC_d^2}$	Parabolic drag parameter
Re_{ref}	Reference Reynolds number at which parameters are determined
f	Reynolds number scaling exponent
C_m	Pitching moment coefficient
M_{crit}	Critical Mach number

Table 6.1: Aerosection input requirements of Xrotor.

Xfoil analysis

To be able to perform an Xrotor analysis, the airfoil characteristics have to be assigned to each blade section. Xfoil is an analysis tool for low Reynolds number airfoils, created by the same developer as Xrotor [66]. Xfoil enables the user to perform viscous and inviscid analysis of a 2D airfoil.

The transition point on the airfoil where the flow transitions from laminar to turbulent flow, is determined by the e^n method in Xfoil. The value of n_{crit} can be varied, which is an indicator of the level of turbulence that is present. By changing the value of n, the turbulence level is altered and the transition over the airfoil is changed. Xfoil has an n_{crit} default value of 9, where a smaller value represents a more turbulent flow and a higher value of n_{crit} results in less turbulence.

In order to make a sensible approximation of the polars using Xfoil, an estimation of the local velocity at each blade section and the corresponding local Reynolds number are determined using Equation 6.2 and Equation 6.3. With the local Reynolds number, a viscous analysis can be performed to obtain the lift and drag polars. It is unnecessary to include the Mach correction in the Xfoil settings, as a Mach correction is already included in the Xrotor routine.

$$V_{loc}(J,r) = \sqrt{V_\infty(J)^2 + (\Omega r)^2} \tag{6.2}$$

$$Re_{loc} = \frac{\rho V_{loc}(J,r)c(r)}{\mu} \tag{6.3}$$

In these equations, the local velocity is represented by V_{loc}, which is dependent on the advance ratio and the radial position of the blade. With the local velocity, the local Reynolds number can be obtained.

The critical Mach number can be estimated using the Prandtl-Glauert relation. The critical Mach number is defined as the Mach number of the free stream at which the local Mach number over an airfoil section becomes equal to 1 [67]. Then, for an arbitrary free stream Mach number, M_∞, the critical pressure coefficient, denoted by $C_{p,crit}$, can be obtained using Equation 6.4. In this equation, γ represents the specific heat ratio and M_∞ corresponds to the free stream Mach number. This equation is used to construct an airfoil independent curve, as presented in Figure 6.3. The airfoil dependent curve is determined through Equation 6.4.

$$C_{p,crit} = \frac{2}{\gamma M_\infty^2}\left[\left(\frac{1+[(\gamma-1)/2]M_\infty^2}{1+(\gamma-1)/2}\right)^{\frac{\gamma}{\gamma-1}} - 1\right] \tag{6.4}$$

$$C_{p\ min} = \frac{C_{p,0\ min}}{\sqrt{1-M_\infty^2}} \tag{6.5}$$

In this equation, $C_{p,0}$ represents the minimum pressure coefficient at the suction side of the airfoil. For the NACA4412 airfoil the critical Mach number is determined at 0.63.

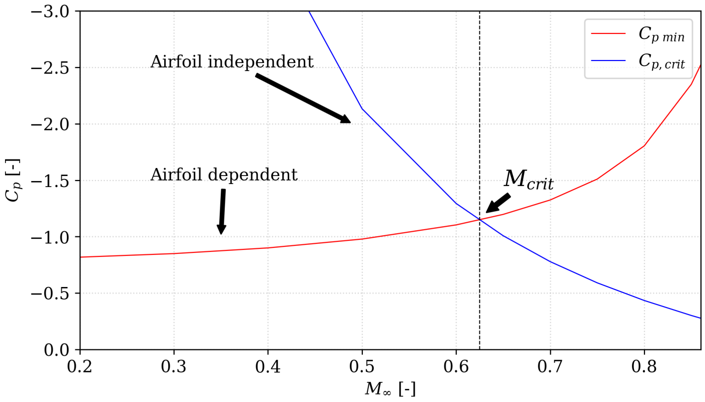

Figure 6.3: Pressure coefficient of the airfoil independent curve and of the airfoil dependent curve plotted against free stream Mach number.

6.2. Quasi-steady modelling

The method used in this thesis to model the unsteady loading on the propeller along the azimuth, is the quasi-steady modelling approach [11]. In a steady simulation, it is assumed that one loading condition of the propeller blade is valid along the azimuth. When an angle of attack of the propeller is introduced, this is no longer the case. To account for the different blade loading encountered by the propeller blade along the azimuth during the unsteady motion of the blade due to the propeller angle of attack, a quasi-steady modelling approach is employed. The quasi-steady modelling approach models the unsteady motion of the propeller, due to an angle of attack by varying the tip speed along the azimuth.

The tip speed is varied along the azimuth, according to Equation 6.6. In this equation, V_F and V_{tip} represent the forward velocity and the velocity of the propeller at the tip, respectively. One angle, α, indicates the propeller angle of attack, while ψ indicates the azimuthal position of the propeller blade during one rotation. In Figure 6.4, a schematic representation is given of the different speeds and corresponding loading along the azimuth.

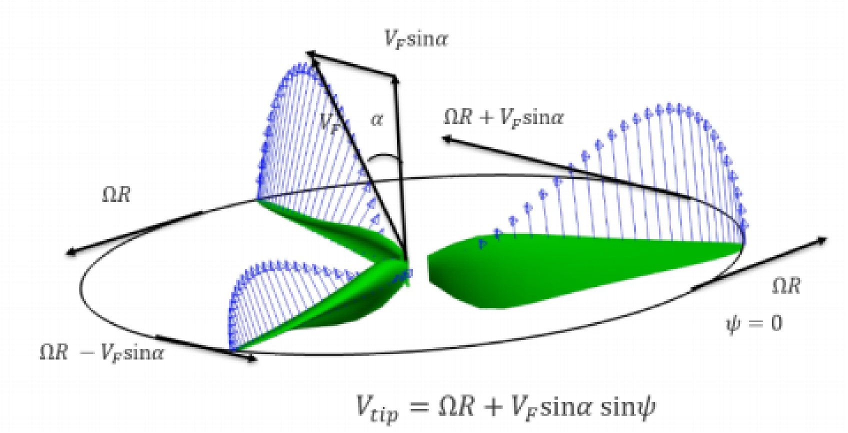
$V_F\sin\alpha$
V_F
α
$\Omega R + V_F\sin\alpha$
ΩR
ΩR
$\psi = 0$
$\Omega R - V_F\sin\alpha$
$V_{tip} = \Omega R + V_F\sin\alpha\,\sin\psi$

Figure 6.4: Blade loading modelled with the quasi-steady loading approach [16].

A flowchart of the quasi-steady loading scheme is presented in Figure 6.5. Multiple steady simulations are run at different tip speeds (given as input to Xrotor in RPM), corresponding to the position of the blade $\psi(i)$. The steady simulation by Xrotor is elaborated on in the previous section. The different blade loadings at the different azimuthal positions are processed in the interface, which combines them into an unsteady blade loading dataset which forms the basis for the unsteady loading noise computation.

In the quasi-steady modelling approach, the unsteady motion of the propeller blade is reduced to a series of steady blade simulations positioned in time. Implementation of this method implies that data obtained

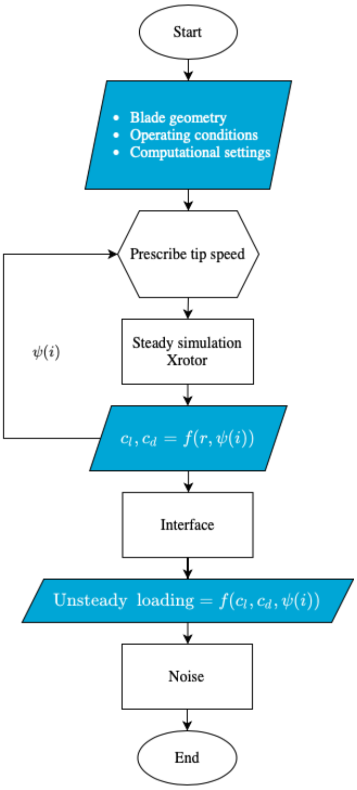

Figure 6.5: Blade section angle definition and components of the velocity triangle, adapted from [2].

for the different azimuthal positions do not take into account any 3D or rotational effects that might translate from one azimuthal blade position to another.

$$V_{tip} = \Omega R + V_F \sin\alpha \sin\psi \tag{6.6}$$

6.3. Tonal noise prediction

Tonal noise produced by a propeller consists of two main components, loading and thickness noise. In this section the working equations of these noise contributions are presented.

6.3.1. Prediction of harmonic loading noise

Tonal noise generated by subsonic propellers can be expressed in the frequency domain by a complex-valued sound pressure amplitude at the m^{th} harmonic of the BPF [59]. By assimilating the individual blade segments into point dipoles the radiation field everywhere in space can be described by Equation 6.7[68].

$$p_{L_{mB}}(\mathbf{x}) = \frac{\mathrm{i}k_{mB}r}{4\pi}\sum_{s=-\infty}^{\infty} F_s(r)\left\{\cos\theta\cos\gamma(r)\mathrm{G}^{(1)}_{mB-s} + \sin\theta\sin\gamma(r)\mathrm{G}^{(2)}_{mB-s}\right\} \tag{6.7}$$

in which

$$\mathrm{G}^{(j)}_n = \frac{\Omega}{2\pi}\int_0^{2\pi/\Omega} \mathrm{G}_j(t)\mathrm{e}^{\mathrm{i}n\Omega t}\,\mathrm{d}t, \quad \mathrm{G}_1(t) = \frac{\mathrm{e}^{\mathrm{i}kR'}}{R^2}\left[1-\frac{1}{\mathrm{i}kR'}\right], \quad \mathrm{G}_2(t) = \sin(\Omega t-\phi)\mathrm{G}_1(t) \tag{6.8}$$

In Equation 6.7, the magnitude of the periodic force acting on the blade element is represented as the complex coefficients, $F_s(r)$, of the Fourier series acting on the blade element. These complex coefficients are called the blade loading harmonics (BLH)[68]. They refer to the sectional integrated forces, which make sense as long as the sources are acoustically compact: the chord lengths are much smaller than the wavelengths of interest ($\frac{c}{\lambda} << 1$). For small-sized UAV rotors with small propeller blade sections, this condition is generally met [59]. The compact condition applies to all blade sections modelled in this thesis. Furthermore, the wavenumber is given by $k_{mB} = mB\Omega/c_0$ and each term of s expresses a spinning radiation mode of angular phase speed $\Omega_s = mB\Omega/(mB-s)$ [69].

Figure 6.6 shows a blade element located at radius r, travelling with a rotational mach number of M. An observer is placed at an arbitrary point in space $\mathbf{x}$, located at a distance of R from the propeller axis. R' represents the distance from the observer to the blade element. The position of the observer is further described in the rotor reference frame with observer angles θ and ϕ. The force exerted by the blade element is given by $F(t)$ where the angle γ represents the angle of the actual fluctuating lift.

6.3.2. Far-field formulation

In Equation 6.9, the far-field formulation is presented. When the acoustic and geometrical far-field condition is met, Equation 6.7 can be simplified to the form presented in Equation 6.9. As soon as the distance between the observer is large when compared both to the diameter of the rotor and the characteristic wavelength of the sound, the rotor can be assumed to be in the far-field. The minimal observation radius is 8 r_{tip} with respect to the propeller centre. Following the approach of Roger [59], by multiplying the observer distance by 2π, a larger value is achieved than the wavelength at the BPF (at an RPM of 4000 about 133.33 Hz).

$$p_{L_{mB}}(\mathbf{x}) = \frac{\mathrm{i}k_{mB}B}{4\pi R}\mathrm{e}^{\mathrm{i}k_{mB}R}\sum_{s=-\infty}^{\infty} F_s(r)\mathrm{e}^{\mathrm{i}(mB-s)(\phi-\pi/2)}\mathrm{J}_{mB-s}(k_{mB}r\sin\theta)\times\left[\cos\theta\cos\gamma(r)-\frac{(mB-s)\sin\gamma(r)}{k_{mB}r}\right] \tag{6.9}$$

$$p_{L_{mB}}(\mathbf{x}) = \frac{\mathrm{i}k_{mB}}{4\pi R}\mathrm{e}^{\mathrm{i}k_{mB}R}BF_0(r)\mathrm{e}^{\mathrm{i}mB(\phi-\pi/2)}\mathrm{J}_{mB}(mBM\sin\theta)\times\left[\cos\theta\cos\gamma(r)-\frac{(mB-s)\sin\gamma(r)}{k_{mB}r}\right] \tag{6.10}$$

where F_s is given by:

$$F_s = \frac{\Omega}{2\pi}\int_0^{2\pi/\Omega} F(t)\mathrm{e}^{\mathrm{i}n\Omega t}\,\mathrm{d}t \tag{6.11}$$

The far-field noise due to the steady-loading noise reduces to the expression presented in Equation 6.10. It differs from the expression in Equation 6.9 in the sense that for steady-loading noise, only the contribution that is associated with the rotor-locked mode, $n = mB$, is taken into account and given by the mean force F_0. When all other BLH, F_s, are taken into account as well, unsteady-loading noise is simulated. The formula assumes that location of the dipole on the blade is located on the e_X axis at the origin of time.

For completeness of the harmonic sound amplitude the steady thickness source is added according to Equation 6.12 [70].

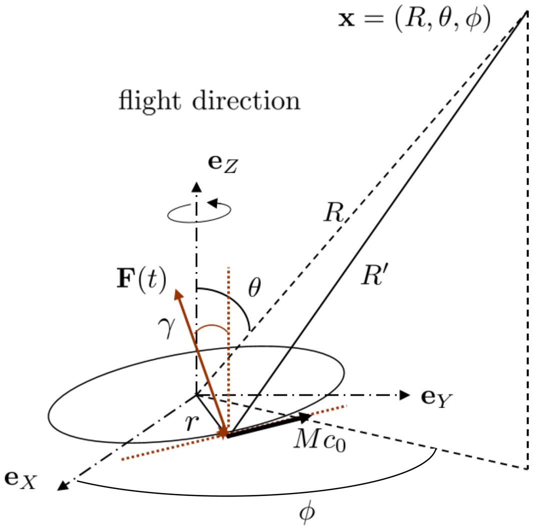

Figure 6.6: System of coordinates for a single blade segment rotating dipole.

$$p_{T_{mB}}(\mathbf{x}) = \frac{iBk_{mB}\Omega\rho_0 c_0}{4\pi R} \mathrm{e}^{\mathrm{i}k_{mB}R} \Delta V_k \mathrm{e}^{\mathrm{i}(mB)(\phi-\pi/2)} J_{mB}(mBM\sin\theta). \tag{6.12}$$

In Equation 6.12, ΔV_k represents the volume of compact blade element k. As the velocity changes around the azimuth, the thickness noise is known to have an unsteady component as well for a rotor at an angle of attack [45]. In this thesis however, only the steady thickness contribution is considered, in both steady and unsteady cases.

7

Synthesis

In this chapter the analytical results are presented and compared with the experimental results. First, a short validation of the steady model is presented. Next, the noise case corresponding to $\alpha_r = 0°$ is presented. In section 6.2, the QS loading is presented together with a study on the BLH harmonics and the Bessel function. Finally, the QS noise results are presented and discussed.

7.1. Steady loading

The data of Xrotor is compared to experimental data obtained for this thesis. The Xrotor simulations are run with 11 local aerodynamic sections defined. The blade geometry is the same as described in chapter 3. The elipsoid blade sections connecting the NACA 4412 sections to the hub are modelled as hub. The design point of the rotors in Xrotor are at $J = 0.4$, meaning that the aerodynamic properties of the propeller are determined using polar data at $J = 0.4$ at the corresponding Reynolds numbers.

It is known from oil flow measurements that a laminar separation bubble exists on the suction side of the blade. In Figure 7.1, it can be observed that a LSB is present. The separation point is indicated by S and the reattachment point is R. A LSB of approximately 45% of the chord at a radial position of 0.6 R indicated by the white dotted line, for a more detailed explanation the reader is referred to the paper of Grande et al. [55]. Three values of n_{crit} are compared in order to establish the transition point from laminar to turbulent with the e^n method. As it is known that a LSB is present, higher values of n_{crit} are presented corresponding to a more laminar flow: $n_{crit} = 5$, corresponding to a turbulence levels of 0.371% and $n_{crit} = 9$, the standard value of Xfoil. These are compared to a value of $n_{crit} = 0.01$, corresponding to a fully turbulent boundary layer.

In Figure 7.2a and Figure 7.2b a comparison is made for different values of J modelled with Xrotor. At the design point $J = 0.4$, all simulations show good agreement with the experiment, as derived from Table 7.1. For a value of $n_{crit} = 9$, a higher thrust is obtained when the propeller is heavily loaded compared to the other two. When the torque coefficient is examined it can be observed that at the design point $J = 0.4$, the simulations with a higher n_{crit} value correspond well to the experimental data while the fully turbulent simulation is slightly lower. In Figure 7.2a, the numerical simulations show an increase deviation from the experimental values from $J > 0.6$, this is assumed to be due to the software as the design point is $J = 0.4$ and the properties are scaled corresponding to J. This holds equally for the torque coefficient. For further simulations a value of

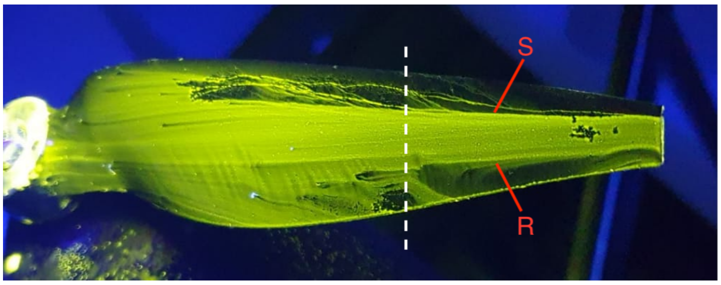

Figure 7.1: Oil flow visualization of the suction side of the blade at RPM= 4000 and $J = 0.4$.

Case	C_T	C_Q
	Value [-]	Value [-]
Experiment	0.0775	0.0083
$n_{crit} = 0.01$	0.0767	0.0076
$n_{crit} = 5$	0.0775	0.0079
$n_{crit} = 9$	0.0784	0.00800

Table 7.1: Thrust and torque coefficient for different values of n_{crit} compared to the experimental values at $J = 0.4$ at RPM = 4000.

$n_{crit} = 5$ is chosen because it matches the thrust and torque coefficients of the design point well.

7.1.1. Discussion

The aerodynamic performance part of the computation is validated using experimental data. In general, a satisfactory agreement is found for the low Reynolds operating conditions. For the advance ratios considered in this section, the propeller based on polars determined with a value of $n_{crit} = 5$, gives good results with respect to the thrust and torque coefficient. The largest difference between the different values of n_{crit} appear in the torque coefficient. However, little variation is found between all the simulations for different values of n_{crit}. The trend variations between the different n_{crit} simulations correspond with literature [3]. It has been noted before in subsection 6.1.1, that the transformation of Xfoil polars to Xrotor aero data is crude, in the sense that the polars must obey a linear and quadruatic fit for the $C_l - \alpha$ and $C_l - C_d$ curve, respectively. For example, any non-linearities in the lift curve at low Reynolds numbers are not well captured [32]. It is assumed here that the crude fitting is the reason for the small deviations between the simulations with different values of n_{crit}.

7.2. Steady noise

In this section the results obtained from the steady noise model are presented and compared to the experimental values. The freestream velocity is coming from the 0° direction and is parallel to the propeller axis.

In Figure 7.3, the steady noise components are presented and compared to the experimental results. The data are obtained at an RPM of 4000 and $J = 0.4$. The observer distance is scaled to a distance of 1.5 m. The total noise is constituted by the lift, drag and thickness noise contribution.

The directivity of BPF 1 is presented in Figure 7.3a. The lift force is the dominant noise source and hence the directivity of the total noise follows the shape of the lift contribution. In correspondence with theory, the dipole shape does not radiate equally in all directions and is symmetric in the propeller axis [71]. The noise radiation of the lift reaches its maximum value of 51.1 dB between $\theta = 90°$ and $\theta = 110°$ above the flightpath and $\theta = 270°$ to $\theta = 250°$ underneath the flightpath. The minima are aligned with the propeller axis corresponding to observer angles of $\theta = 0°$ and $\theta = 180°$. The thickness noise is symmetrical in the propeller axis and reaches its maximum value at 37.1 dB at $\theta = 90°$ and $\theta = 270°$. A similar profile is found for the noise contribution from the drag with a maximum value of 32.4 dB. The total harmonic noise is found to be 53.4 dB at 90°. The experimental value at this angle is found 55.4 dB and hence a difference of 2 dB is found at BPF 1.

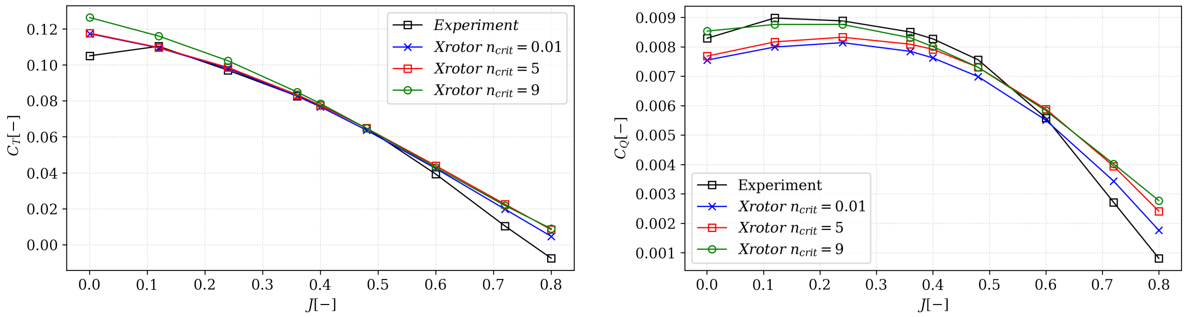

(a) Comparison of thrust coefficients obtained with Xrotor for different values of n_{crit}.

(b) Comparison of torque coefficients obtained with Xrotor for different values of n_{crit}.

Figure 7.2: Xrotor simulation comparison with experimental results at RPM= 4000 for different values of J.

The levels of the experiment appear to correspond well from $\theta = 60°$ to $130°$ in terms of both magnitude and shape. From $50°$ to $60°$ the experimental values decrease at a quicker rate than the numerical values.

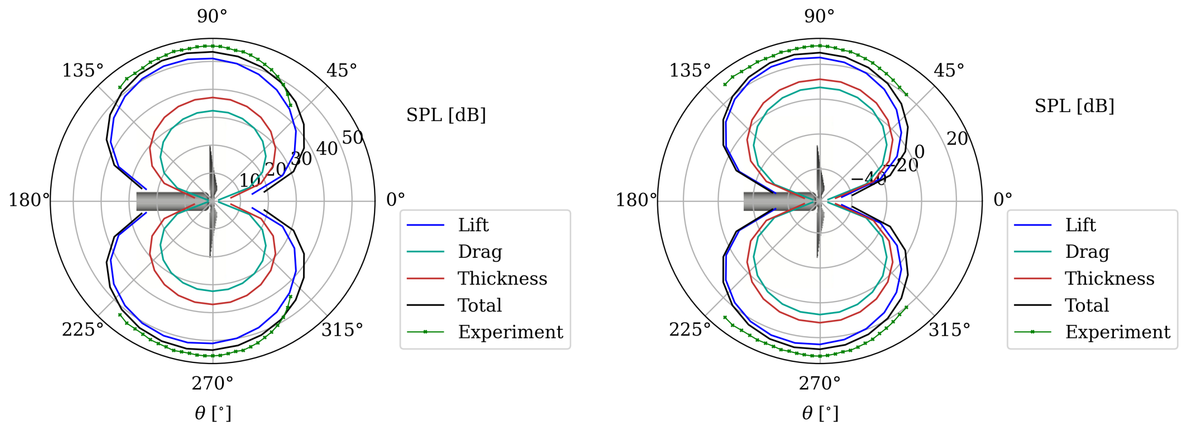

(a) Lift, drag and thickness noise at BPF 1 compared with the experimental results.

(b) Lift, drag and thickness noise at BPF 2 compared with the experimental results.

Figure 7.3: Noise obtained at $J = 0.4$, RPM= 4000 at a distance R of 1.5 m for BPF 1 and 2 for $\alpha_r = 0°$.

The directivity of BPF 2 is presented in Figure 7.3b both numerically and experimentally. When the numerical solution is compared to BPF 1, similarities in shape can be identified for all noise contributions. The magnitude is, as expected, lower when compared to BPF 1. The shape of the total numerical noise seems to follow the shape of the experimental data for most of the observer angles. Towards the edges however, at $\theta = 120°$ to $\theta = 130°$, the deviation in magnitude increases. Similarly, this can be observed from $\theta = 220°$ to $\theta = 230°$. Overall, the noise is underpredicted by the steady model with an average of 4 dB.

A comparison of the BPF and its multiples with respect to the spectrum obtained with mic_{14} is given in Figure 7.4. The distance of mic_{14} is scaled to 1.5 m from the propeller centre and the numerical noise data is presented accordingly. When the first 5 BPF tones are compared to the spectrum, an almost linear decrease of the predicted harmonic noise is observed of about 26 dB per harmonic. It can be observed that at the first two BPF the noise is underpredicted by a small margin. From BPF 3 onwards, the underprediction increases and at BPF 4 and 5 the contribution of the numerical components are very small. The contribution of each of the noise sources linearly decreases with increasing BPF. When the experimental steady loading noise is compared to the theoretical noise it can be observed that the peaks persist at higher BPF frequencies than those predicted by the theory. The cause of this is believed to be flow non-uniformity and is said to be responsible for the conflict between theory and experiment here [60].

7.2.1. Remarks on the steady analysis

In this section, satisfactory correspondence was found between the experimental and numerical data at BPF 1. For higher harmonics the correspondence decreases but this is expected as BPF 1 is mainly dominated by the steady loading contribution [59], [60].

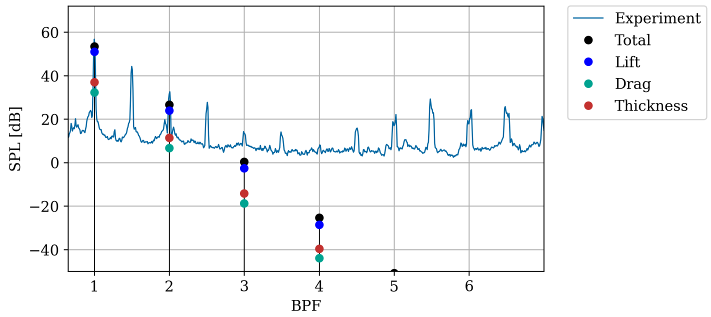

Figure 7.4: Lift, drag and thickness noise at the first 5 BPF compared to the spectrum measured with mic_{14}, $R = 1.5$ m, $fr = 1.11$ Hz.

7.3. Quasi-steady analysis

In this section the quasi-steady analysis is presented. First, an overview of the loading along the azimuth is presented. Next, a noise analysis is presented showing how the noise profile is affected by the quasi-steady loading.

7.3.1. Quasi-steady loading

For the QS loading cases the azimuth is discretized in 24 sections. For brevity, only the 24 discretization is elaborated on. As mentioned in section 6.2, the variation in tip speeds is given as input to Xrotor in RPM. Hence, in Figure 7.5, the variation in prescribed RPM is presented for different rotor angles of attack. The steady case, where the RPM is constant along the azimuth, is presented as reference, which features for 4000 RPM and a freestream velocity of 8 m/s a total thrust of 3.42 N.

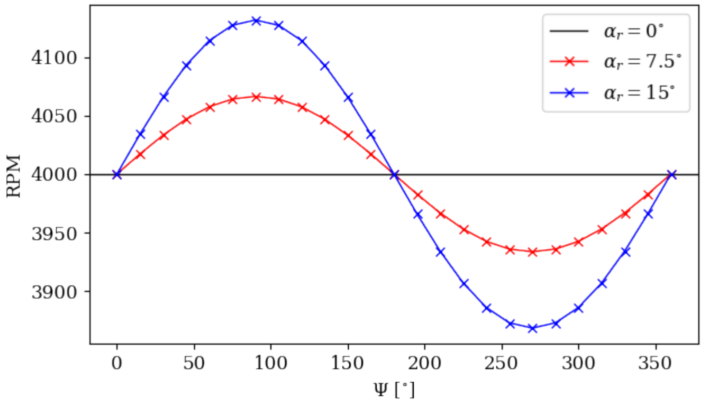

Figure 7.5: Azimuthal variation of the RPM of the propeller for different values of α_r.

For a rotor angle of attack of $\alpha_r = 15°$ a maximum value of 4131.8 RPM and minimum value of 3868.2 RPM are prescribed around the azimuth corresponding to a thrust of 1.94 N on the advancing blade (at azimuthal position $\Psi = 90°$) and 1.6 N on the retreating blade ($\Psi = 270°$), respectively. The thrust corresponding to 4000 RPM is 1.755 N ($\Psi = 0°$ & $\Psi = 180°$)[1]. For $\alpha_r = 7.5°$, the minimum and maximum RPM value are 3933.5 RPM and 4066.5 RPM, corresponding to a a thrust of 1.645 N on the retreating blade ($\Psi = 270°$) and 1.805 N on the advancing blade ($\Psi = 90°$), respectively. The thrust corresponding to 4000 RPM is 1.725 N ($\Psi = 0°$ & $\Psi = 180°$).

The variation of the sectional thrust coefficient (per unit span) along the azimuth is presented in Figure 7.6, for a rotor at both $\alpha_r = 7.5°$ and $\alpha_r = 15°$ in two isocontour plots in the rotor plane. The direction of rotation is counter clock-wise and the field of vision is above the rotor. The respective high and low-thrust regions are found at the azimuthal positions corresponding with those of the RPM at $\Psi = 90°$ and $\Psi = 270°$, matching with the advancing and retreating side of the blades, respectively. The variations in force on the blade, presented in Figure 7.6, are associated with unsteady-loading.

In order to establish if this is a reasonable estimate of variation in loading along the azimuth a comparison is made with a high-fidelity simulation. The simulation is performed using Dassault Systèmes PowerFLOW which encompasses a lattice Boltzmann very large eddy simulation approach. The simulation is performed at an RPM of 6000 and $J = 0.4$, corresponding to a freestream velocity of 12 m/s and a rotor angle of attack of 15°. The blade is tripped at 25% from the leading edge. For further details about the simulation the reader is referred to [72]. The steady thrust was found to be 3.4 N per blade. At $\alpha_r = 15°$, the thrust force varies between 4.3 N at $\Psi = 107°$ (maximum) and 2.8 N at $\Psi = 288°$. Consequently, when the difference between the maximum and minimum is normalized with respect to the steady thrust, a 44% variation in loading is found along the azimuth. When the similar case is run, using the QS loading scheme, the thrust force varies between 3.88 N at $\Psi = 90°$ (maximum) and 3.18 N at $\Psi = 270°$ (minimum), resulting in a thrust variation of 21%.

---

[1] The forward velocity, V_f, is split up into an axial and tangential component. Consequently, the thrust for the unsteady case is higher at 4000 RPM when compared to the steady case.

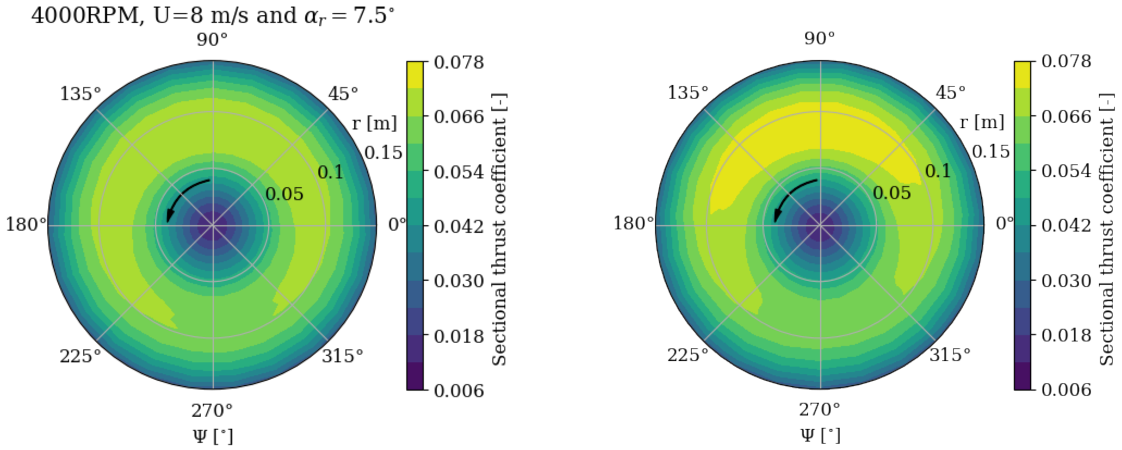

(a) $\alpha_r = 7.5^\circ$.

(b) $\alpha_r = 15^\circ$.

Figure 7.6: Isocontour of the sectional thrust coefficient at $J = 0.4$ and RPM= 4000 for different rotor angles of attack.

7.3.2. Discussion

The QS loading scheme works in the sense that it shows variation in loading along the azimuth. The locations of maximum and minimum thrust are $\Psi = 90^\circ$ and $\Psi = 270^\circ$. For $\alpha_r = 7.5^\circ$ at an RPM of 4000 and $J = 0.4$, a variation in RPM of 3.3% leads to a variation in loading around the azimuth of 9.7%. When the angle of attack is increased to $\alpha_r = 15^\circ$, the variation in RPM increases to 6.8% and the variation in loading increases to 21%.

When compared to the high-fidelity approach it becomes clear that the QS model approximation of the variation in loading along the azimuth is less than half of the high-fidelity approach. At an RPM of 6000 and $J = 0.4$ and $\alpha_r = 15^\circ$ the difference in loading along the azimuth of the high-fidelity approach is 44%, that of the QS loading approach 21%. It can be concluded that the QS loading scheme can be employed for simple analyses, related to an early design phase where simplicity is traded for accuracy.

7.4. Quasi-steady loading noise

In this section the quasi-steady loading noise results are discussed. First, in subsection 7.4.1 some properties of the far-field noise formulation are discussed. Second, the noise results are presented in subsection 7.4.2.

7.4.1. Blade loading harmonics and the Bessel function

In order to asses the QS loading noise the BLH are determined. The absolute value of the BLH of the lift force are presented in Figure 7.7. The BLH are obtained by aligning the azimuthal loading case, $\Psi = 90^\circ$, with the e_x axis in Figure 6.6. Only the first ± 3 BLH are considered in this thesis. In Figure 7.7a, the BLH of the propeller at a rotor angle of attack of $\alpha_r = 7.5^\circ$ are presented. The steady component, F_0, is the dominant harmonic with a maximum value corresponding to 0.109. From the figure it can be derived that the BLH $F_{\pm1}$ have a magnitude of about 2.3 % of the steady contribution. At a rotor angle of $\alpha_r = 15^\circ$, the maximum value of the steady component is roughly the same as for the smaller rotor angle of attack at 0.112. The BLH of order ±1 have a magnitude of 4.4 % when compared to the steady contribution. Here it becomes clear that a larger rotor angle of attack increases the unsteady loading contribution.

Equation 6.9 states that the complex-valued pressure amplitude noise is dependent on the Bessel function which operates as a radiation-efficiency factor. To illustrate the effect of the Bessel function, it is plotted as an efficiency factor of the magnitude $mB \cdot J_{mB}(mB \cdot X)$, with $X = M\sin\theta$, for the steady-loading contribution in Figure 7.8 (a). When an observer angle of $\theta = 90^\circ$ is assumed, X corresponds to the Mach number of the rotating force given in the legend. The Mach number of $X = 0.175$, corresponding to the red line resembles a tip speed Mach number of a rotor blade at 4000 RPM and a rotor radius of 0.15 m. The function, F, is given as a function of the BPF and its multiples where its magnitude is given in decibels. The vertical lines indicate the first 3 BPF corresponding with $(m = 1)$, $(m = 2)$ and $(m = 3)$. When the red line in Figure 7.8 (a) is examined, a decay of 21 dB for the steady loading is found between BPF 1 and BPF 2 and for every step in BPF afterwards.

In Figure 7.7, the blade loading harmonics of the first three modes (±) are presented. The contribution of unsteady loading mainly originates from the $|F_{\pm1}|$ BLH. To gain more insight in the radiation efficiency

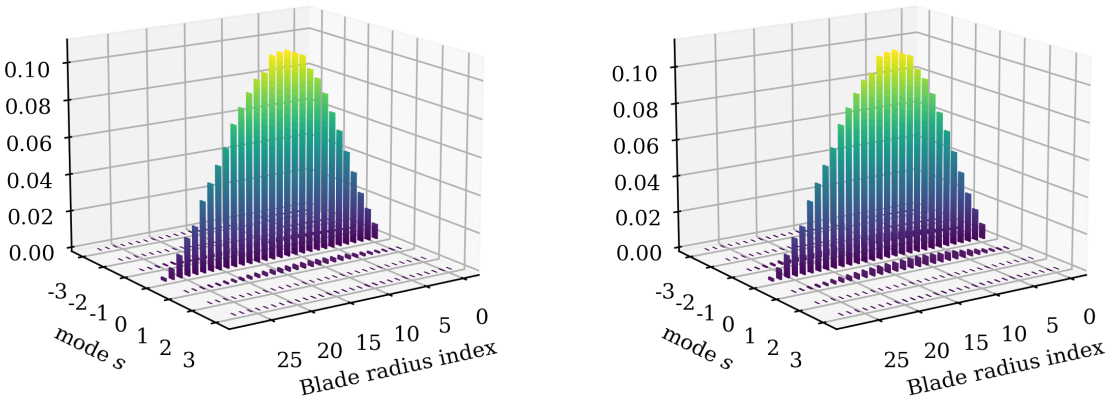

(a) BLH obtained at $\alpha_r = 7.5°$.

(b) BLH obtained at $\alpha_r = 15°$.

Figure 7.7: Absolute value of the BLH at $\alpha_r = 7.5°$ and $\alpha_r = 15°$.

of these modes, the Bessel functions of the modes $s = 1$ and $s = -1$ are evaluated in Figure 7.8, (b) and (c) respectively. When $J_{mB-1}(mB \cdot X)$ is evaluated it can be observed that the radiation efficiency factor of the mode $s = 1$ exceeds the steady contribution of the Bessel function. For example, at BPF 1 the relative difference between the steady and the $s = 1$ mode is 20.6 dB. Steady loading noise dominates BPF 1 harmonic, but the efficiency factor rapidly decreases. Consequently, unsteady loading noise is expected to overwhelm the steady loading noise from BPF 2 up to higher harmonics. Furthermore, the contribution of the $J_{mB+1}(mB \cdot X)$ can be neglected because it will never overwhelm the steady loading noise contribution.

7.4.2. Quasi-steady Noise

In this section the noise results obtained with the QS scheme for the loading are presented. First, the rotor at an angle of attack of $\alpha_r = 7.5°$ is discussed after which the $\alpha_r = 15°$ case is presented. Finally, some remarks

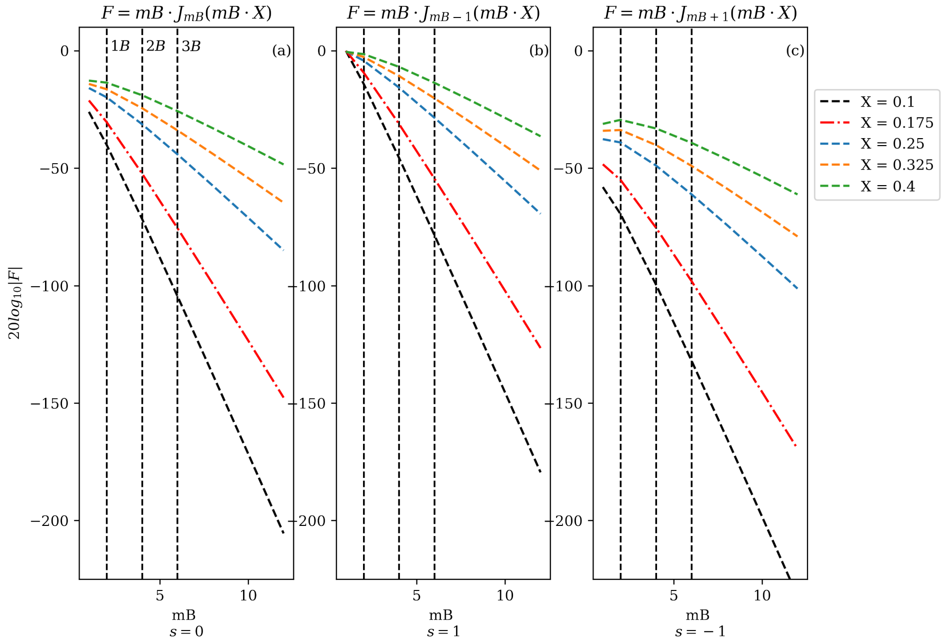

Figure 7.8: Bessel function factors of steady loading noise (a) and of the first order, $s = 1$ and $s = -1$, harmonics of unsteady loading noise in (b) and (c).

BPF index	Steady [dB]	$QS_{\theta=90^\circ}$ [dB]	$QS_{\theta=270^\circ}$ [dB]
1	53.17	54.42	55.45
2	26.13	29.75	31.31
3	-0.36	11.44	13.57
4	-26.34	-13.0	-11.05
5	-51.98	-38.24	-36.43
6	-77.38	-63.7	-61.8

Table 7.2: SPL values of the steady case compared to the QS case at $\alpha_r = 7.5^\circ$ at observer positions $\theta = 90^\circ$ and $\theta = 270^\circ$.

on the analyses presented here are made.

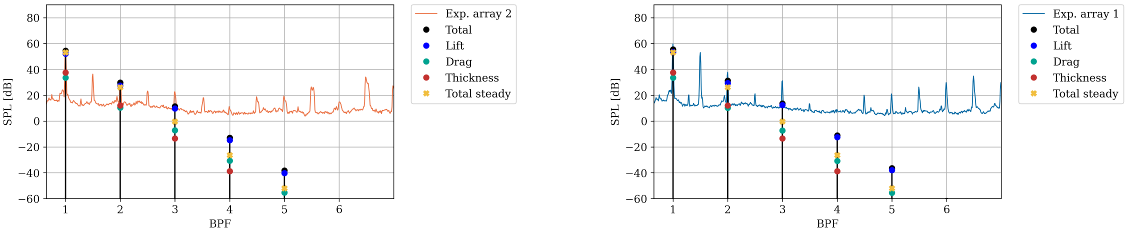

(a) Spectrum obtained with array 2 at observer angle $\theta = 90^\circ$.

(b) Spectrum obtained with array 1 at observer angle $\theta = 270^\circ$.

Figure 7.9: Spectrum obtained with mic_{14} compared to the harmonics of the BPF obtained with steady and QS model at RPM= 4000, $\alpha_r = 7.5^\circ$, $J = 0.4$ and R = 1.5 m.

The spectra measured with array 2 and array 1, at $\alpha_r = 7.5^\circ$, are presented in Figure 7.9a and Figure 7.9b, respectively. Furthermore, the contributions of the QS noise model are plotted at the BPF and its multiples, together with the total noise of the steady case. When the total noise of the QS simulation is compared to the total noise of the steady simulation, indicated by the yellow cross, two observations can be made: for an observer angle of 90°, in Figure 7.9a, similar values are found for BPF 1 for the QS case at 54.4 dB and the steady case at 53.2 dB. This difference increases slightly for BPF 2 to a difference of 3.7 dB. For BPF 3 a difference of 11.8 is found, increasing to 13.7 at BPF 5. When compared to the observer angle of 270°, in Figure 7.9b, slightly larger SPL values are found for the QS noise due to the tilt of the rotor, as can be seen in Table 7.2.

For the rotor at an angle of attack of $\alpha_r = 15^\circ$, the spectra together with the numerical results are plotted in Figure 7.10 for two observer positions. Similar observations can be made as with the $\alpha_r = 7.5^\circ$ case however a couple of remarks are in place: the tilt of the rotor is increased and hence the values found for $\theta = 90^\circ$ in Table 7.3 are lower when compared to the $\alpha_r = 7.5^\circ$, in Table 7.3. The opposite effect can be observed for $\theta = 90^\circ$. When the QS numerical results of the two figures are compared, a slight increase of the SPL values can be observed at an angle of 270°.

7.4.3. Discussion

The variation of the loading around the azimuth, determined with the QS model, leads to BLH harmonics of the first order with a magnitude of 2.3% and 4.4% of the steady loading noise for $\alpha_r = 7.5^\circ$ and $\alpha_r = 15^\circ$,

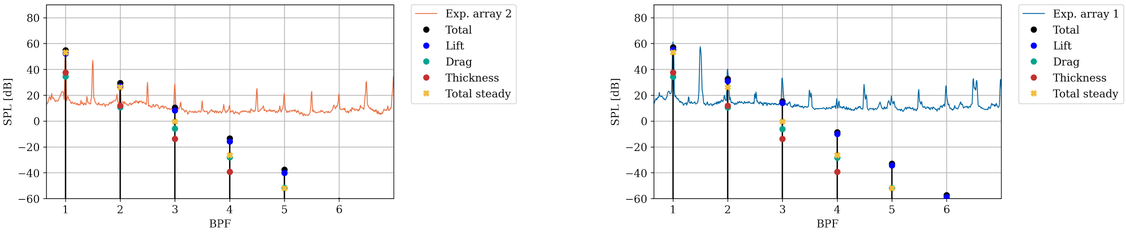

(a) Spectrum obtained with array 2 at observer angle $\theta = 90^\circ$.

(b) Spectrum obtained with array 1 at observer angle $\theta = 270^\circ$.

Figure 7.10: Spectrum obtained with mic_{14} compared to the harmonics of the BPF obtained with steady and QS model at RPM= 4000, $\alpha_r = 15^\circ$, $J = 0.4$ and R = 1.5 m.

BPF index	Steady [dB]	$QS_{\theta=90^\circ}$ [dB]	$QS_{\theta=270^\circ}$ [dB]
1	53.17	54.7	57.02
2	26.13	29.44	32.55
3	-0.36	10.36	15.26
4	-26.34	-13.39	-8.66
5	-51.98	-37.59	-32.96
6	-77.38	-61.85	-57.37

Table 7.3: SPL values of the steady case compared to the QS case at $\alpha_r = 15^\circ$ at observer positions $\theta = 90^\circ$ and $\theta = 270^\circ$.

respectively. The magnitude of the BLH increases with angle of attack, this is expected as the unsteady loading contribution rises with an increasing variation in velocity around the azimuth. The contribution of the QS loading increases the SPL with respect to the steady case for both above and underneath the flightpath. The difference between the steady and QS noise becomes larger as higher BPF harmonics are considered. This is mainly due to the decay rate of the Bessel function.

Furthermore, when a spectral comparison is made, the higher harmonics are still under predicted for all harmonics above the BPF 1. Although an increase is observed for the SPL of the higher BPF harmonics when a rotor angle of attack is considered, it seems that the measure at which the unsteady loading noise contribution underestimates the contribution to the higher harmonics. It is known that the QS loading model underestimates the amount of loading variation along the azimuth, however, it is unknown to which extent the prescription of the variation in tip speed is responsible or that different causes for unsteadiness play a part as well.

Using the method described in section 6.3 means that the complex pressure amplitude is a superposition of the different BLH components. In the QS model, the forward velocity is decomposed into an axial and tangential component. Effectively this means that $F_{0_{QS}}$ is larger than $F_{0_{steady}}$, because of the reduced inflow velocity. Furthermore, the velocity effect is not taken into account, which would alter the radiation efficiency of the noise above and underneath the flightpath [9], [45]. Considering these arguments means that a decrease in noise of the QS case with respect to the steady case can not reasonably be expected. Similarly to what was found in the experiment, unsteady loading noise may lead to an increase in noise levels everywhere, but the modulation of the noise is different above and underneath the propeller [63]. Furthermore, the thickness noise component is expected to also contain an unsteady contribution which is not included in the analysis [9].

8

Conclusion & Recommendations

A small UAV rotor has been subjected to angular inflow in order to investigate the effect of unsteady loading on the blade due to the variation in velocity around the azimuth. The rotational velocity was set to 4000 RPM and the operating condition was $J = 0.4$, corresponding to a freestream velocity of 8 m/s. A compact dipole frequency domain formulation has been implemented in order to model the noise contribution emitted by steady and unsteady loading on the blade. A compact monopole frequency domain formulation has been implemented to model the harmonic contribution of the noise known as thickness noise. These results have been compared with experimental data from acoustic measurements in an anechoic tunnel. The conclusions from the results can be broadly divided into a an experimental and analytical part, related to the hypotheses and research questions presented in chapter 2.

1. What is the change in noise spectrum of a low Reynolds number, fixed pitch propeller when an unsteady motion is introduced by varying the angle of attack of the propeller from 0° to 7.5° and 15°?

    (a) What is the change in the harmonic noise contribution when a propeller angle of attack is introduced? *The variation in tip speed along the azimuth is expected to result in the onset of unsteady loading, resulting in more pronounced tonal noise.*

    It was was found that when the rotor is placed at an angle of attack with respect to the inflow the harmonic noise increases for an observer underneath the flightpath compared to axial-inflow conditions. This confirms hypothesis 1.

    It was found that when that when the rotor is placed at an angle of attack with respect to the inflow the harmonic noise decreases for an observer above the flightpath when compared to axial-inflow conditions. This confirms hypothesis 2.

    (b) How do the spectra measured directly above and underneath the flightpath compare? *When the rotor is tilted with respect to the freestream a difference in loading and radiation efficiency is expected above and underneath the flightpath.*

    For the first two harmonics of the BPF a clear difference between the above and underneath the flight path can be observed. Overall an increase in the first two harmonics of the spectrum is observed for both $\alpha_r = 7.5°$ and $\alpha_r = 15°$ when the observer is located underneath the flightpath. When the observer is positioned above the flightpath a decrease of the first two harmonics of the BPF is observed. The 3 BPF is consistently higher when the rotor is at an angle of attack when compared to the steady case both for underneath and above the flightpath.

    (c) How do the different propeller angles of attack compare to each other? *The variation in tip speed along the azimuth changes with rotor angle of attack.*

    When the OASPL of the first 6 BPFs is examined, a clear increase of the OASPL underneath the flightpath is observed when the rotor angle of attack is increased. The opposite is true for an observer placed above the rotor.

2. How is the harmonic noise component affected by the unsteady motion, introduced by a small angle of attack of the propeller when it is modelled by a quasi-steady modelling approach?

(a) What is the change in blade loading along the azimuth when a propeller angle of attack is introduced? *The radiated noise due to unsteady loading is the related to the variation in blade loading.*

The maximum blade loading at a rotor angle of attack of $\alpha_r = 15°$, corresponding to a maximum RPM value of 4131.8 of the advancing blade, is 1.94 N. The minimum blade loading, corresponding to the retreating blade moving at an RPM value of 3868.2, is 1.6 N. This means that a variation in blade loading of 21% is found along the azimuth. The thrust corresponding to 4000 RPM is 1.755 N per blade.

The maximum blade loading at a rotor angle of attack of $\alpha_r = 7.5°$, corresponding to a maximum RPM value of 3933.5 of the advancing blade, is 1.805 N. The minimum blade loading, corresponding to the retreating blade moving at an RPM value of 3933.5, is 1.645 N. This means that a variation in blade loading of 9.7% is found along the azimuth. The thrust corresponding to 4000 RPM is 1.725 N per blade.

(b) What is the change in the loading noise contribution when different angles of attack of the rotor are considered? *The change in noise contribution is an indicator of the variation in loading along the azimuth.*

It was found that the change in loading noise contribution increases when the rotor angle of attack is increased. For higher harmonics, the contribution of the unsteady loading noise becomes more important.

(c) How does the prediction of the harmonic spectrum compare to the experimental harmonic spectrum? *Relates to the applicability of the modelling approach.*

When a rotor angle of attack of $\alpha_r = 0°$, corresponding to the steady case, is considered, a difference of 2.4 dB at the 1 BPF is observed for an observer placed directly above or underneath the flightpath. The magnitude of the the higher harmonics decreases linearly with 26 dB.

When the rotor is placed at an angle of attack $\alpha_r \neq 0°$ the harmonics of the spectrum corresponding to above the flightpath are underestimated for BPF 2 to 6. The 1 BPF is overpredicted. The harmonics corresponding to the spectrum underneath the flightpath are underpredicted from BPF 1 to 6. Furthermore, the difference in SPL associated with above and underneath the flightpath is only due to the tilt of the rotor.

8.1. Recommendations

Experimental

1. In order to obtain acoustic measurements of better quality, it is advised to separate the configurations for acoustic measurements and loading measurements. The set-up described in section 3.3 exists of a nacelle containing the motor, propeller and loadcell. In order for the loadcell to operate correctly, the loadcell has to be the only point of contact between the motor propeller system and the nacelle. During the experiments it was noticed that excessive motor and structure noise were present during the acoustic measurements. In order to isolate the noise emitted by the propeller, a set-up consisting of two separate configurations is proposed: one in which the loads can be measured and the noise emissions are not of importance. Another, in which the motor is securely clamped in a structure, minimising structural vibrations induced by the propeller.

2. In order to characterize the RPM variability, the use of an encoder is advised. The pressure signal can be related to the measured variation in RPM and hence the variation in dB due to the variability in RPM of the set-up can be expressed. Similar procedure has been followed in [55].

3. In order to asses the noise level variation between different measurements, baseline measurements are proposed in future research that help define the variation in measured noise levels between different measurements.

Analytical

1. It is advised to not use Xrotor for future implementations. Xrotor is not easy to troubleshoot when, for example, input errors are given. Furthermore, the data output is limited: e.g, the angle of attack is not part of the standard output of the programme. It is advised to use or write a programme of which the source-code can be altered and of which the output variables can be determined by the user. This would also improve the flow of data and get rid of inconveniently formatted text documents.

2. To capture the directivity of the propeller in a more accurate way with a frequency domain method, it is recommended to use a source mode expansion [68]. This method can be directly coupled to the loading per azimuthal position output of the quasi-steady modelling scheme. Furthermore, this approach would include the near-field contribution and hence would be valid everywhere in space. Instead of modelling the acoustic field of a rotating dipole, a circular distribution of stationary phase-shifted dipoles can be positioned on a circle. The circle distribution can be discretized in N sections having the properties corresponding to their azimuthal position [73]. This approach is extensively used by Moreau and Roger [59] [69].

3. Instead of the source mode expansion a time-domain approach would also capture this effect. The acoustically compact source approximation would still be valid. The QS modelling output can be listed and linked to time in order to create the time history of the blade loading. This can be used as input for the time-domain formulation of the compact acoustic dipole and monopole for loading and thickness noise, respectively [16].

4. Additions to the method used in this thesis would include an unsteady thickness source and the expansion of the compact dipole formulation to include the velocity effect, as given by Hanson [45] [9].

A

Post-Processing Experimental Data

In this appendix, some of the post-processing methods are briefly elaborated on.

A.1. Data post processing routines

A.1.1. Loadcell performance measurements

The ATI Mini40 loadcell returns 6 voltages corresponding to the forces and moments in all Cartesian coordinates. The measured voltages were converted to the actual moments and forces produced by the propeller in a number of steps:

1. *Application of calibration matrices*
   Before acquiring the loadcell data, the calibration matrix provided with the loadcell is loaded into Labview. The measured signal stored in the data files is the calibrated data.

2. *Offset determination of the loadcell*
   The data acquired with the loadcell displayed a non-zero value in unloaded conditions. This is because the motor, hub etc., were also attached to the loadcell. In order to account for this offset bias, measurements were taken at the beginning ($n_m = 1$) and at the end of all zero-angle of attack measurements ($n_m = N_m$) and for all angle of attack measurements. Two bias measurements were taken for both zero-propeller and non-zero angle of attack. The results of the bias measurements were averaged to obtain the mean bias for all signals, Equation A.1.

$$F_{i_{bias}} = \frac{\left(\frac{1}{N}\sum_{j=1}^{N}(F_i)_j^{n_m=1} + \frac{1}{N}\sum_{j=1}^{N}(F_i)_j^{n_m=N_m}\right)}{2} \tag{A.1}$$

3. *Mean loads determination*
   A similar averaging is also applied to the data set containing the data during propeller operation:

$$F_{i_{raw}} = \frac{1}{N}\sum_{j=1}^{N}(F_i)_j^{n_m=1} \tag{A.2}$$

4. *Correcting the loading data for bias*
   By correcting the loadcell data with the bias, the actual loads exerted by the propeller on the loadcell are obtained.

$$\Delta F_i = F_{i_{raw}} - F_{i_{bias}} \tag{A.3}$$

   In this equation, ΔF_i represents the average of the propeller forces and moments measured by the loadcell.

A.1.2. Propeller noise measurements

1. *Power Spectral Density calculation with Welch's method*

   The calibrated microphone signal is used to calculate the power spectral density with Welch's method, as incorporated by the scipy module in python [53]. The method of Welch consists of dividing the time history of the input signal into a number of segments. These segments may or may not overlap. The different segments are Fourier transformed, after which the periodogram for each segment is calculated. Finally, the average is taken over all the segments to obtain a final approximation of PSD for the entire time history.

   Splitting the time history of the signal into different segments over which is averaged has the benefit that it produces a smaller variance of the PSD estimate when compared to a calculation that uses the entire time history of the signal in one calculation. On the other hand, Welch's method also results in shorter data records, which reduces the resolution of PSD estimates. When using Welch's method, one should always consider that there is a trade-off between the reduction of the variance and the resolution.

   Below, some of the steps taken by Welch are briefly addressed [53]. In order to obtain the PSD, the data set, X(j), j = (0, 1,..., N-1) is divided into K amount of segments which each have length L. The starting point of each segment is denoted by distance D, as given in Equation A.4.

$$\begin{aligned} X_1(j) &= X(j) & j &= 0,\dots,L-1 \\ X_2(j) &= X(j+D) & j &= 0,\dots,L-1 \\ X_K(j) &= X(j+(K-1)D) & j &= 0,\dots,L-1 \end{aligned} \tag{A.4}$$

   By taking the discrete Fourier transform, the segmented time series are all converted to the frequency domain.

$$A_k(n) = \frac{1}{L}\sum_{j=0}^{L-1} X_k(j)W(j)\mathrm{e}^{-2\mathrm{i}\frac{jkn}{L}} \qquad k = 1,2,\dots,K \tag{A.5}$$

   In this equation, i is the imaginary number and W is the window function. The window function is applied to each segment of the time series. A Hann window is used in the current analysis.

   Next, the modified periodograms I are computed for each segment, indicated by k, using the transformed Fourier data.

$$I_k(f_n) = \frac{L}{U}|A_k(n)|^2 \qquad k = 1,2,\dots,K \tag{A.6}$$

   With f_n and U defined by:

$$\begin{aligned} f_n &= \tfrac{n}{L} \quad n = 0,1,\dots,\tfrac{L}{2} \\ U &= \tfrac{1}{L}\textstyle\sum_{j=0}^{L-1} W^2(j) \end{aligned} \tag{A.7}$$

   The spectral estimate of the input signal is then determined by taking the average of over all segments:

$$\hat{P}(f_n) = \frac{1}{K}\sum_{k=1}^{K} I_k(f_n) \tag{A.8}$$

2. *Computation of the Sound pressure Levels*

   The estimate of the power spectral density of the input signal is used to determine the sound pressure level.

$$SPL(f_n) = 10log_{10}\left(\frac{\hat{P}(f_n)\Delta f}{p_0^2}\right) \tag{A.9}$$

   In this equation, Δf represents the frequency bin width. The variable p_0 is the acoustic reference pressure and has a value of 20μPa. The window length is chosen such that a frequency resolution ranging from 1 to 3 Hz was obtained.

The OASPL is calculated according to:

$$\text{OASPL} = 10\log_{10}\left[\left(\int_{f_{min}}^{f_{max}} \text{PSD}(f)\,\mathrm{d}f\right)/\,p_{\text{ref}}^2\right] \tag{A.10}$$

Bibliography

[1] M. Drela and H. Youngren. Xrotor user guide, 2003.

[2] M. Drela. Qprop theory document, 2006. [Online] available at: `web.mit.edu/drela/Public/Qprop` [Accessed 30 November 2020].

[3] R. W. Deters, G. K. Ananda Krishnan, and M. S. Selig. Reynolds number effects on the performance of small-scale propellers. In *32nd AIAA applied aerodynamics conference*, page 2151, 2014.

[4] B. McGrahan. *Surface Oil Flow Measurements on Several Airfoils at Low Reynolds Numbers*. M.s. thesis, University of Illinois at Urbana-Champaign, Urbana, IL, 2003.

[5] L. L. M. Veldhuis. *Propeller wing aerodynamic interference*. PhD thesis, Delft University of Technology, 2005.

[6] H. H. Hubbard. *Aeroacoustics of flight vehicles: theory and practice*, volume 1. NASA Office of Management, Scientific and Technical Information Program, 1991.

[7] T. F. Brooks, D. S. Pope, and M. A. Marcolini. Airfoil self-noise and prediction, 1989.

[8] M. Takallu and V. Lessard. Periodic blade loads of a high speed propeller at small angle of attack. In *27th Joint Propulsion Conference*, page 2250, 1991.

[9] D. Hanson. Sound from a propeller at angle of attack: a new theoretical viewpoint. *Proceedings of the Royal Society of London. Series A: Mathematical and Physical Sciences*, 449(1936):315–328, 1995.

[10] J. Frota, P. Lempereur, and M. Roger. Computation of the noise of a subsonic propeller at an angle of attack. In *4th AIAA/CEAS Aeroacoustics Conference*, page 2282, 1998.

[11] B. E. Zolbayar. Investigation noise from electric, low-tip-speed aircraft propellers. Master's thesis, The Pennsylvania State University, 2018.

[12] Y. Yang, Y. Liu, Y. Li, E. Arcondoulis, Y. Wang, W. Li, and B. Huang. Aerodynamic and aeroacoustic characteristics of a multicopter propeller during forward flight. In *2018 Joint Propulsion Conference*, page 4892, 2018.

[13] Y. Yang, Y. Liu, Y. Li, E. Arcondoulis, and Y. Wang. Aerodynamic and aeroacoustic performance of an isolated multicopter rotor during forward flight. *AIAA Journal*, 58(3):1171–1181, 2020.

[14] W. AG. *Operator's manual Clinotronic plus: The intelligent universal inclinometer*. Im Hölderli, CH-8405 Winterthur, Switzerland, 2016.

[15] A. I. Automation. Six-axis force/torque sensor system installation and operation manual. 2020.

[16] K. S. Brentner. Challenges of extremely quiet propulsion. Presentation, Sustainable Aviation Symposium, San-Francisco, 2018.

[17] A. Hawkins. *FT31755 Calibration Certificate and Accuracy Report*. ATI Industrial Automation. Serial Number: FT31755.

[18] A. Momont. Ambulance drone, 2020. [Online] available at: `https://www.tudelft.nl/en/ide/research/research-labs/applied-labs/ambulance-drone/` [Accessed 9 September 2020].

[19] B. Mishra, D. Garg, P. Narang, and V. Mishra. Drone-surveillance for search and rescue in natural disaster. *Computer Communications*, 156:1–10, 2020.

[20] F. Al-Turjman. *Unmanned Aerial Vehicles in Smart Cities*. Springer, 2020.

[21] X. Wang, A. Chowdhery, and M. Chiang. Skyeyes: adaptive video streaming from uavs. In *Proceedings of the 3rd Workshop on Hot Topics in Wireless*, pages 2–6, 2016.

[22] S. Watkins, J. Burry, A. Mohamed, M. Marino, S. Prudden, A. Fisher, N. Kloet, T. Jakobi, and R. Clothier. Ten questions concerning the use of drones in urban environments. *Building and Environment*, 167: 106458, 2020.

[23] D. Floreano and R. J. Wood. Science, technology and the future of small autonomous drones. *Nature*, 521(7553):460–466, 2015.

[24] N. Mohamed, J. Al-Jaroodi, I. Jawhar, A. Idries, and F. Mohammed. Unmanned aerial vehicles applications in future smart cities. *Technological Forecasting and Social Change*, 153:119293, 2020.

[25] E. A. S. Agency. Introduction of a regulatory framework for the operation of unmanned aircraft systems in the 'open' and 'specific' categories. Opinion No 01/2018, 2018.

[26] N. Kloet, S. Watkins, and R. Clothier. Acoustic signature measurement of small multi-rotor unmanned aircraft systems. *International Journal of Micro Air Vehicles*, 9(1):3–14, 2017.

[27] K. S. Brentner and F. Farassat. Modeling aerodynamically generated sound of helicopter rotors. *Progress in Aerospace Sciences*, 39(2-3):83–120, 2003.

[28] R. K. Shenoy, F. W. Kohlhepp, and K. P. Leighton. Acoustic characteristics of 1/20-scale model helicopter rotors. Contractor report 177355, NASA, 1986.

[29] N. S. Zawodny, D. D. Boyd Jr, and C. L. Burley. Acoustic characterization and prediction of representative, small-scale rotary-wing unmanned aircraft system components. In *72nd American Helicopter Society (AHS) Annual Forum*, 2016.

[30] M. Cerny and C. Breitsamter. Investigation of small-scale propellers under non-axial inflow conditions. *Aerospace Science and Technology*, page 106048, 2020.

[31] M. McCrink and J. W. Gregory. Blade element momentum modeling of low-re small uas electric propulsion systems. In *33rd AIAA Applied Aerodynamics Conference*, page 3296, 2015.

[32] J. Winslow, H. Otsuka, B. Govindarajan, and I. Chopra. Basic understanding of airfoil characteristics at low reynolds numbers (10 4–10 5). *Journal of Aircraft*, 55(3):1050–1061, 2018.

[33] R. H. Self. Propeller noise. *Encyclopedia of Aerospace Engineering*, 2010.

[34] O. Gur and A. Rosen. Design of quiet propeller for an electric mini unmanned air vehicle. *Journal of Propulsion and Power*, 25(3):717–728, 2009.

[35] D. Casalino. An advanced time approach for acoustic analogy predictions. *Journal of Sound and Vibration*, 261(4):583–612, 2003.

[36] D. B. Hanson and M. R. Fink. The importance of quadrupole sources in prediction of transonic tip speed propeller noise. *Journal of Sound and Vibration*, 62(1):19–38, 1979.

[37] G. J. Ruijgrok. *Elements of aviation acoustics*. Delft University Press, 1993.

[38] D. Casalino. *Analytical and numerical methods in vortex-body aeroacoustics*. PhD thesis, Politecnico di Torino et Ecole Centrale de Lyon, 2002.

[39] F. Farassat and G. P. Succi. The prediction of helicopter rotor discrete frequency noise. *American Helicopter Society (AHS)*, pages 497–507, 1982.

[40] D. Kurtz and J. Marte. A review of aerodynamic noise from propellers, rotors, and lift fans. *Technical Report 32-1462*, 1970.

[41] G. Sinibaldi and L. Marino. Experimental analysis on the noise of propellers for small uav. *Applied Acoustics*, 74(1):79–88, 2013.

[42] P. Candeloro, T. Pagliaroli, D. Ragni, and S. Di Francesco. Small-scale rotor aeroacoustics for drone propulsion: a review of noise sources and control strategies, 2019.

[43] G. Yakhina, M. Roger, S. Moreau, L. Nguyen, and V. Golubev. Experimental and analytical investigation of the tonal trailing-edge noise radiated by low reynolds number aerofoils. In *Acoustics*, volume 2, pages 293–329. Multidisciplinary Digital Publishing Institute, 2020.

[44] E. Arcondoulis, C. Doolan, A. Zander, and L. Brooks. A review of trailing edge noise generated by airfoils at low to moderate reynolds number. *Acoustics Australia*, 38(3), 2010.

[45] D. B. Hanson and D. J. Parzych. Theory for noise of propellers in angular inflow with parametric studies and experimental verification, 1993.

[46] M. Goldstein. Unified approach to aerodynamic sound generation in the presence of solid boundaries. *The Journal of the Acoustical Society of America*, 56(2):497–509, 1974.

[47] Q. Henricks, Z. Wang, and M. Zhuang. Small-scale rotor design variables and their effects on aerodynamic and aeroacoustic performance of a hovering rotor. *Journal of Fluids Engineering*, 142(8), 2020.

[48] T. Delft. A-tunnel. [cited 20 Jan 2021). URL https://www.tudelft.nl/lr/organisatie/afdelingen/aerodynamics-wind-energy-flight-performance-and-propulsion/facilities/low-speed-wind-tunnels/a-tunnel/.

[49] R. Merino-Martínez, A. R. Carpio, L. T. L. Pereira, S. van Herk, F. Avallone, D. Ragni, and M. Kotsonis. Aeroacoustic design and characterization of the 3d-printed, open-jet, anechoic wind tunnel of delft university of technology. *Applied Acoustics*, 170:107504, 2020.

[50] D. Hanson. Noise radiation of propeller loading sources with angular inflow. In *13th Aeroacoustics Conference*, page 3955, 1990.

[51] G. S. . Vibration. Gras 40 ph ccp free-field array microphone, 2020. [Online] available at: https://www.grasacoustics.com/products/special-microphone/array-microphones/product/ss_export/pdf2?product_id=178 [Accessed 24 December 2020].

[52] C. E. Tinney and J. Sirohi. Multirotor drone noise at static thrust. *AIAA Journal*, 56(7):2816–2826, 2018.

[53] P. Welch. The use of fast fourier transform for the estimation of power spectra: a method based on time averaging over short, modified periodograms. *IEEE Transactions on audio and electroacoustics*, 15(2): 70–73, 1967.

[54] R. MacNeill and D. Verstraete. Blade element momentum theory extended to model low reynolds number propeller performance. *The Aeronautical Journal*, 121(1240):835–857, 2017.

[55] E. Grande, G. Romani, D. Ragni, F. Avallone, and D. Casalino. Aeroacoustic investigation of a propeller operating at low-reynolds numbers. *Unpublished*, 2021.

[56] E. Sarradj, C. Fritzsche, T. Geyer, and J. Giesler. Acoustic and aerodynamic design and characterization of a small-scale aeroacoustic wind tunnel. *Applied Acoustics*, 70(8):1073–1080, 2009.

[57] R. McKay and M. J. Kingan. Multirotor unmanned aerial system propeller noise caused by unsteady blade motion. In *25th AIAA/CEAS Aeroacoustics Conference*, page 2499, 2019.

[58] D. L. Huff and B. S. Henderson. Electric motor noise for small quadcopters: Part 1–acoustic measurements. In *2018 AIAA/CEAS Aeroacoustics Conference*, page 2952, 2018.

[59] M. Roger and S. Moreau. Tonal-noise assessment of quadrotor-type uav using source-mode expansions. In *Acoustics*, volume 2, pages 674–690. Multidisciplinary Digital Publishing Institute, 2020.

[60] M. E. Goldstein. Aeroacoustics. *New York*, 1976.

[61] N. Gourdain, T. Jardin, R. Serre, S. Prothin, and J.-M. Moschetta. Application of a lattice boltzmann method to some challenges related to micro-air vehicles. *International Journal of Micro Air Vehicles*, 10 (3):285–299, 2018.

[62] R. WOODWARD. Measured noise of a scale model high speed propeller at simulated takeoff/approach conditions. In *25th AIAA Aerospace Sciences Meeting*, page 526, 1987.

[63] T. Sinnige, D. Ragni, A. M. Malgoezar, G. Eitelberg, and L. L. Veldhuis. Apian-inf: an aerodynamic and aeroacoustic investigation of pylon-interaction effects for pusher propellers. *CEAS Aeronautical Journal*, 9(2):291–306, 2018.

[64] S. Goldstein. On the vortex theory of screw propellers. *Proceedings of the Royal Society of London. Series A, Containing Papers of a Mathematical and Physical Character*, 123(792):440–465, 1929.

[65] M. Drela. Propeller characterization for qprop, 2005. [Online] available at: `http://web.mit.edu/drela/Public/web/qprop/prop_measure.pdf` [Accessed 21 November 2020].

[66] M. Drela. An analysis and design system for low reynolds number airfoils. conf. procs. In *Conference on Low Reynolds Number Airfoil Aerodynamics, University of Notre Dame, France*, 1989.

[67] J. D. Anderson Jr. *Fundamentals of aerodynamics*. Tata McGraw-Hill Education, 2010. 722-737.

[68] M. Roger and S. Moreau. Aeroacoustic installation effects in cooling fan systems part 1: Scattering by surrounding surfaces. In *Proceedings of the International Symposium on Transport Phenomena and Dynamics of Rotating Machinery, Honolulu, HI, USA*, pages 17–22, 2008.

[69] M. Roger. On combined propeller synchronization and edge scattering for the noise reduction of distributed propulsion systems. In *Proceedings of the 26th International Congress on Sound and Vibration, Montreal, Canada*, pages 7–11, 2019.

[70] S. Glegg and W. Devenport. *Aeroacoustics of low Mach number flows: fundamentals, analysis, and measurement*. Academic Press, 2017.

[71] D. A. Russell, J. P. Titlow, and Y.-J. Bemmen. Acoustic monopoles, dipoles, and quadrupoles: An experiment revisited. *American journal of physics*, 67(8):660–664, 1999.

[72] A. Pandey. *Investigation of propeller characteristics at low Reynolds number with an angle of attack*. M.s. thesis, TU Delft, 2021.

[73] K. Kücükcoskun. *Prediction of free and scattered acoustic fields of low-speed fans*. PhD thesis, Ecole Centrale de Lyon, 2012.